

Natural variations in underwater noise levels in the Eastern Grand Banks, Newfoundland.

by

© *Kanachi Angadi*

A thesis submitted to the School of Graduate Studies in partial fulfilment of the
requirements for the degree of

Master of *Science*

Memorial University of Newfoundland

Department of *Physics and Physical Oceanography*

July 2019

St. John's

Newfoundland

July 2019

Abstract

“The topic of underwater noise pollution due to oil & gas exploration is a genuine concern to scientists and researchers. Studying acoustic propagation from noise sources has become one of the standard environmental impact assessment criteria for offshore developments. Lower level noise is also a concern when persistent and higher than naturally occurring background noise. The natural environment contributes sound through wind and wave motion, currents, precipitation, and sea ice. A two-month autonomous acoustic monitoring program was conducted in 2015 on the Grand Banks, as part of a study to understand the impact of seismic surveys off the coast of Newfoundland. This study aims to use that data to improve our understanding of the ambient soundscape and relate the observations to known relationships between noise levels and wind and rainfall rates. A challenge with the present data is that the observations are made in shallow water where bottom and surface reflections act to increase expected natural sound levels. This increase in sound levels interferes with algorithms used to relate wind and rain to noise levels. An analytical model was used to adjust noise levels accounting for the shallow water environment. The corrected data were evaluated using algorithms for Weather classification developed by Nystuen which were used to identify the data points with sound levels associated with shipping, drizzle, rain and near surface bubbles. The shipping contamination was removed from the data sets and resulting sorted data was used to estimate wind speeds that were compared to independent observations obtained from model data provided by Department of Fisheries and Oceans, Canada.”

Acknowledgements

Firstly, I would like to express my sincere gratitude to my supervisor Dr. Len Zedel for the continuous support of my studies at Memorial University and related research, for his patience, motivation, and immense knowledge. His guidance helped me in all the time of research and writing of this thesis. I could not have imagined having a better advisor and mentor for my research studies. My sincere thanks to Bruce Martin and Christopher Whitt from JASCO Applied Sciences for taking out time to discuss and share information pertaining to the data. My sincere thanks also goes to Dr. Jinshan from Department of Fisheries and Oceans, Canada, Newfoundland and Dr. Entcho Demirov from Memorial University, who helped me understand the wind model data that I have worked with for my thesis. I would like to thank Andrew Kim from School of Graduate studies for his continued support throughout my study period. I would also like to thank Dr. David Barclay for answering my questions and helping me understand my research better. I wish to thank Chris Stevenson for his timely support which helped me finish my thesis. I thank all faculty members, my colleagues and friends in the department for the stimulating discussions and a special thanks to Heather Andres for organizing the departmental seminars which made me work hard before deadlines. Last but not the least, I would especially like to thank my family. My husband, Chakravarthy has been very supportive of me throughout this entire process. My parents, Vijaya and Late Dr. Sudhakara Rao Angadi, for their continued support and encouragement. My siblings, Mridula and Bhavani for having faith in me. I dedicate my thesis to my beloved son Deep.

Contents

Abstract	ii
Acknowledgements	iii
List of Tables	vii
List of Figures	viii
1 Introduction	1
2 Background	4
2.1 Introduction	4
2.1.1 Terminology	5
2.1.2 Transmission loss	6
2.1.3 Ray tracing concept	8
2.1.4 Attenuation	12
2.1.5 Measurements of underwater sound	13
2.2 Signal processing	15
2.2.1 Sampling theorem & DTFT (Discrete Time Fourier Transform) . . .	16

2.2.2	Power spectral density (PSD)	17
2.2.3	Welch's method	19
2.3	Ambient noise	21
2.3.1	Ship traffic	25
2.3.2	Biological sources	26
2.3.3	Surface agitation	27
2.3.4	Seismic activity	28
2.3.5	Breaking of ice	28
2.3.6	Rain	29
2.3.7	Shallow and deep water ambient noise	31
2.3.8	Ambient noise levels as a function of depth	32
3	Nystuen weather classification	34
3.1	Introduction	34
3.2	Algorithm for weather classification	34
3.2.1	Check for excess low frequency sound	35
3.2.2	Check for high frequency sound - heavy rain	37
3.2.2.1	Test 1 - Heavy rain	38
3.2.2.2	Test 2 - Heavy rain	38
3.2.3	Check for drizzle	39
3.2.4	Check for bubbles present	41
3.2.5	Wind speed algorithm	42
4	Bottom interaction model	44
4.1	Introduction	44

4.2	Surface and bottom interactions	46
4.3	Summary	49
5	Data methods and results	54
5.1	Data acquisition	54
5.1.1	PGS survey track	55
5.2	Analysis and results	57
5.2.1	Averaging method	66
5.2.2	Standard deviation approach	73
5.2.3	Comparison with GDPS (Global Deterministic Prediction System) wind model data	76
6	Conclusions	82
	Bibliography	86

List of Tables

5.1	Deployment and retrieval dates along with locations for the AMARs	56
-----	---	----

List of Figures

2.1	Deep-water sound velocity profile. (Adapted with permission from [15]) . . .	9
2.2	Geometry for reflection, transmission, and refraction of plane waves at an interface of two different material media.	11
2.3	Receiver sensitivity graph of AMAR hydrophone	15
2.4	Autonomous Multichannel Acoustic Recorder	15
2.5	Wenz curves describing pressure spectral density levels of marine ambient noise from weather, wind, geologic activity, and commercial shipping for deep water conditions. (Adapted with permission from [7] [35])	23
2.6	Categories of sea state and wind speed and the effects to the Sea Surface. (Adapted with permission from [35])	24
2.7	Examples of the spectral signals for different geophysical sound sources observed from the data from an ocean surface mooring in the South China Sea. (Adapted with permission from [20])	30
2.8	The average deep water ambient noise spectra. (Adapted with permission from [33])	31
3.1	20 kHz sound Vs. 4 kHz sound levels. (Adapted with permission from [25])	36

3.2	Rain detection test using 5 kHz and 20 kHz. (Adapted with permission from [25])	37
3.3	Drizzle detection test using 8 kHz and 20 kHz. (Adapted with permission from [25])	40
3.4	Bubble detection test using 5 kHz and 25 kHz. (Adapted with permission from [25])	42
4.1	Basic model of surface generated sound	45
4.2	Geometry of image sources used in modeling multiple surface and bottom reflected rays	48
4.3	Effects of instrument placement, and bottom characteristics on received signal. Response is indicated in dB relative to source levels at the surface. a) No bottom reflections, only the effects of acoustic absorption are considered, depths of 125 m, 250 m, 500 m and 1000 m are shown. b) Bottom effect; examples of how the received signal at a depth of 100 m is altered by the presence of a (0 dB loss) bottom at depths of 500 m to 4000 m. c) Bottom effects; receiver is positioned on the bottom at a depth of 30 m, bottom attenuations of -4 dB, -6 dB, -8 dB and -10 dB are shown.	50
4.4	Spectrum of received sound at 100 m depth as caused by (white) surface generated ambient sound	52
5.1	Map showing locations of AMAR stations DFO-CT and DFO-ST	56
5.2	AMAR in-line mooring diagram	57
5.3	Power spectrum created using un-averaged transformed data (red) when compared to an averaged Welch's PSD (blue)	58

5.4	Spectrogram view at site DFO-ST	60
5.5	Comparison of Sound Pressure Level (SPL) values at sites DFO-CT and DFO-ST for sampling frequency 64 kHz	61
5.6	Comparison of Sound Pressure Level (SPL) values at sites DFO-CT and DFO-ST for sampling frequency 375 kHz	62
5.7	Model response in dB for the entire frequency range at site DFO-ST at sampling frequency 375 kHz	63
5.8	Comparison of Sound Pressure Level (SPL) values at site DFO-CT with Model response at sampling frequency 64 kHz	64
5.9	Comparison of Sound Pressure Level (SPL) values at site DFO-ST with Model response at sampling frequency 64 kHz	64
5.10	Comparison of Sound Pressure Level (SPL) values at site DFO-CT with Model response at sampling frequency 375 kHz	65
5.11	Comparison of Sound Pressure Level (SPL) values at site DFO-ST with Model response at sampling frequency 375 kHz	65
5.12	Comparison after model response at site DFO-CT (in green) and site DFO- ST for sampling frequency 64 kHz	65
5.13	Comparison after model response at site DFO-CT and DFO-ST at sampling frequency 375 kHz	65
5.14	3 hourly averages for shipping contamination detection at DFO-CT (with- out correction)	67
5.15	3 hourly averages for shipping contamination detection at DFO-ST (with- out correction)	67

5.16	3 hourly averages for shipping contamination detection at DFO-CT (with correction)	68
5.17	3 hourly averages for shipping contamination detection at DFO-ST (with correction)	68
5.18	3 hourly averages for rainfall detection at DFO-CT	69
5.19	3 hourly averages for rainfall detection at DFO-ST	69
5.20	3 hourly averages for drizzle detection at DFO-CT	69
5.21	3 hourly averages for drizzle detection at DFO-ST	69
5.22	3 hourly averages for bubble detection at DFO-CT	70
5.23	3 hourly averages for bubble detection at DFO-ST	70
5.24	Wind speeds vs Time in days at DFO-ST (without bottom interaction model correction)	71
5.25	U10 (m/s) vs effect of 3 dB change in sound pressure level at 8 kHz	72
5.26	Wind speeds vs Time in days at DFO-ST	73
5.27	Standard deviation plot sorted from low to high values	74
5.28	DFO-CT sound pressure levels before and after the Standard deviation approach (sampling frequency 64 kHz)	75
5.29	Model wind speeds vs observed at DFO-CT	77
5.30	Model wind speeds vs observed at DFO-ST	78
5.31	Model wind speeds vs observed at DFO-CT without bottom interaction model corrections	78
5.32	Scatter plot comparing wind speeds at DFO-CT	79
5.33	Scatter plot comparing wind speeds at DFO-CT without bottom interaction model corrections	80

Chapter 1

Introduction

In the past, ocean noise was only considered as a factor that limited operational performance of military sonar systems. In fact, the foundational research on the topic is essentially pursued from that perspective. More recently, it has become obvious that ocean noise not only impacts human applications of underwater sound but it is of critical importance to marine life. That recognition has generated a demand for better understanding of both natural and anthropogenic ocean noise levels. In this thesis, I focus on noise levels observed on the Grand Banks of Newfoundland. A variety of factors influence the sound levels on the Grand Banks. The natural environment contributes sound through wind and wave action, currents, precipitation and sea ice. Sounds produced by marine mammals, fish and invertebrates have a significant influence on the local soundscape. Anthropogenic activities also affect sound levels off Newfoundland. Over the past decade, the oil and gas industry has expanded on Canada's east coast, resulting in a plethora of sounds associated with exploration and extraction activities. A project was initiated by Department of Fisheries & Oceans (DFO) to understand the effects of seismic exploration on the Snow Crabs

that are found in abundance in the waters off Newfoundland. In support of this research, JASCO Applied Sciences partnered with DFO to investigate the ambient soundscape at a site where the seismic effects on Snow Crabs was tested and sound levels were predicted from a planned seismic exposure. This thesis aims to establish the baseline underwater sound levels at the two sites in Grand Banks and identify the natural variations contributed by rain and wind.

This thesis is organised as follows:

Chapter 2, is a detailed literature background on various basic concepts of sound produced underwater, ray tracing, transmission loss, ambient noise and various sources of ambient noise, signal processing techniques etc.

In Chapter 3, Nystuen's weather classification algorithm is explained to categorize the ambient sound contributed by shipping, rain, drizzle and ambient bubbles by incorporating the various test conditions under each category.

The main objective of Chapter 4, was to address the naturally occurring effects that result from bottom reflections and acoustic absorptions. The effects of surface and bottom have been investigated with a simple analytical model of ocean ambient sound generation at the surface by incorporating image sources.

In Chapter 5, data from Grand Banks was analyzed. Two data sets were available for the two sites of interest. The data from both the sites, DFO-CT and DFO-ST, were studied and wind speeds were obtained for the entire data set for the period of deployment. Three hourly averages of the sound pressure levels were obtained from the entire data set and the sound pressure levels corresponding to shipping, rain, drizzle and ambient bubbles were identified for both the sites and flagged accordingly. We chose to measure the standard deviation of sound levels in each data set and sort them to identify the outliers. Standard

deviation approach proved to be a good approach to understand the occurrences of very high wind speeds, owing to the fact that there were transient high energy pulses in narrow band frequencies at both the sites.

Chapter 6 is the conclusions chapter that discusses and draws conclusion to this thesis work.

Chapter 2

Background

2.1 Introduction

Sound is a mechanical wave comprising of pressure oscillations through a compressible medium. A given sound wave is described, in part, by the frequency (f) and amplitude of the wave. The frequency of the wave determines the perceived pitch which means, higher frequencies are associated with higher pitches. The amplitude on the other hand is related to what is considered as loudness. The wavelength (λ) is related to the frequency and the speed of sound by the relation $\lambda = c/f$, where c is the speed of sound. It is well known that the speed of sound is dependent on the properties of a medium like elastic modulus and density of the medium. In case of fluids, it is given as $c = \sqrt{\frac{K}{\rho}}$, where K is the bulk modulus of the fluid and ρ is the density of the fluid. In air the speed of sound for compressional waves is approximately 300 m/s whereas in water it is 1500 m/s.

In the ocean, sound is trapped between the surface and the bottom. The ocean surface

is a simple horizontal boundary and often a nearly perfect reflector. Whereas, the oceanic floor is a lossy boundary with a strongly varying topography across the ocean basins. Scattering and attenuation of sound is caused due to the small-scale roughnesses associated with both the boundaries. The structure of the ocean bottom depends on the local geology. In general, the deep ocean is considered to consist of a thin stratification of sediments overlying the oceanic crust in contrast to the thick stratification over the continental crust on the continental shelves.

2.1.1 Terminology

Pressure levels associated with the acoustic measurements usually vary over many orders of magnitude. Hence, it is very common convention to report acoustic measurements in units of decibels. Decibels is a unit that requires an arbitrary reference value. The widely accepted convention in the field of underwater acoustics is to use $1 \mu\text{Pa}$ as the reference pressure in water while the reference pressure in air being $20 \mu\text{Pa}$. Sound pressure level is defined as the ratio of the Root Mean Square (RMS) pressure squared to the square of the reference pressure. In decibels, the Sound pressure is expressed by Equation 2.1.

$$SPL(dB) = 10\log\frac{p_{rms}^2}{p_{ref}^2} = 20\log\frac{p_{rms}}{p_{ref}} \quad (2.1)$$

Where p_{rms} is the root mean square pressure and p_{ref} is the reference pressure amplitude. If the measurements are made in air then reference pressure amplitude $p_{ref} = \text{dB re } 20 \mu\text{Pa}$ and if made in water then $p_{ref} = \text{dB re } 1 \mu\text{Pa}$

Sound intensity can be found as

$$I = \frac{p^2}{\rho c} \quad (2.2)$$

where p is the RMS pressure in Pa (Pascals) obtained from measurements, ρ is density in kg/m^3 and c is the sound speed in m/s. The denominator of Equation 2.2 is also known as the specific acoustic impedance. It is the opposition of a medium to wave propagation, and it depends on the medium properties and the type of wave propagating through the medium. Thus, the acoustic impedance that is acting in opposition to the wave propagation increases with an increase in medium density as well as an increase in the speed of sound. Direct calculation of intensity from Equation 2.2 assumes that the wave is a plane wave. Also the Intensity level (IL) is

$$IL = 10 \log\left(\frac{I}{I_o}\right) \quad (2.3)$$

where the reference intensity of sound in water is $I_o = 6.5 \times 10^{-19} \text{ W/m}^2$. This being the reason why air and water measurements in decibels (dB) are not the same as the references differ by 62 dB. Ideally, acousticians would be able to measure intensity directly, but practically, it is easier to measure and detect changes in pressure and then convert these into intensities. If both Sound Pressure Level (SPL) and Intensity Level (IL) are quoted in dB (decibels), they are *equivalent*.

2.1.2 Transmission loss

The acoustic signal of the ocean becomes distorted due to multipath effects and weakened due to various loss mechanisms. Multipath formation in the ocean is determined by two important effects, one is the sound that gets reflected at the surface, at the bottom, at any objects and also the refraction of sound in the water. The refraction of sound in water is

more evident in deep water channels due to the variation of sound speed with depth. In underwater acoustics context, any variation in signal strength with range is considered as Transmission Loss (TL). Geometric spreading is a very significant source of transmission loss. The rate of losses due to spreading can be classified as spherical and cylindrical. In spherical spreading, the source exists in a lossless, boundless medium with homogenous properties. A spherical wave is produced by a source which propagates at the same speed in each direction. The total acoustic power must be conserved as the spherical wave expands. Based on the surface area of a spherical wave ($4\pi r^2$, where r is the radius) the intensity of the wave decreases as r^2 . On the other hand, the power of an expanding wave in a cylindrical environment with rigid boundaries, the power must be conserved as no power is transmitted through the boundaries. For the surface area of a cylinder, $2\pi rH$, r being the radius and H being the depth, the intensity of the wave decreases as a function of r . The Transmission Loss terms can be converted to corresponding terms. In case of spherical spreading, Transmission Loss is $TL = 20\log_{10}(r)$ while for cylindrical spreading, it is $TL = 10\log_{10}(r)$, when the reference distance is 1 meter. Transmission loss together with other terms can be grouped together into SONAR parameters. SONAR is an acronym for Sound Navigation and Ranging. This is a technology that was developed as a means of tracking enemy submarines during World War II. A SONAR consists of a transmitter, transducer, receiver and display unit. SONAR parameters are determined by the *equipment*, the *medium*, and the *target*. These parameters are levels in units of decibels relative to the standard reference intensity of a $1 \mu\text{Pa}$ plane wave.

2.1.3 Ray tracing concept

Sound velocity in the ocean varies with depth due to changes in density and temperature, reaching a local minimum near a depth of 800 – 1000 meters. This local minimum, called the SOFAR (Sound Fixing and Ranging) channel, acts as a structure that guides waves (waveguide), as sound tends to bend towards it. Ray tracing may be used to calculate the path of sound through the ocean up to very large distances, incorporating the effects of the SOFAR channel, as well as reflections and refractions off the ocean surface and bottom. From this process, locations of high and low signal intensity may be computed, which are important in the fields of ocean acoustics. The speed of sound through water has been found to be mainly a function of three factors. They are temperature, pressure or depth and salinity. Because the speed is not constant, sound does not travel along straight paths. The dependance of speed of sound on temperature, salinity and depth is given by approximately Equation 2.4 [22].

$$c = 1449.2 + 4.6T - 0.055T^2 + 0.00029T^3 + (1.34 - 0.010T)(S - 35) + 0.016z \quad (2.4)$$

where c = speed of sound (m/s)

T = Temperature (degC)

S = Salinity, (parts per thousand)

z = depth (m)

The speed of sound has information about the ocean environment. The speed of sound as well as sound speed profiles affect the propagation and attenuation rate of sound. Figure 2.1 gives a typical deep-water sound speed profile in oceans. A plot of sound speed as a function of depth, is called the Sound Velocity Profile (SVP), and it is the fundamental tool for predicting how sound will travel. Neglecting salinity, the SVP can be obtained from

sampling the ambient temperature at various depths. An inexpensive probe to do this is called an expendable bathythermograph (XBT).

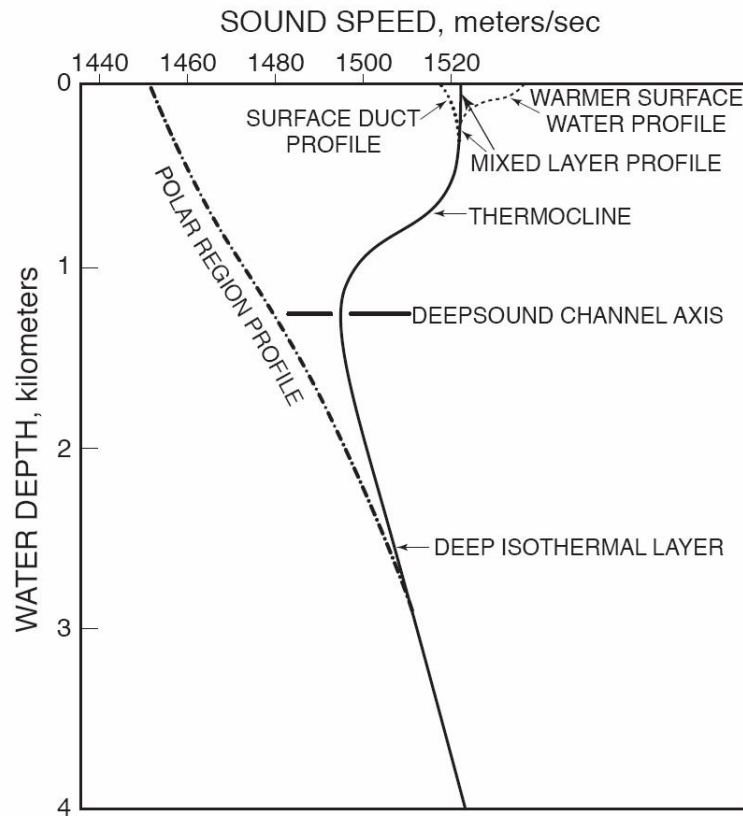


Figure 2.1: Deep-water sound velocity profile. (Adapted with permission from [15])

The deep water sound velocity profile can be divided into four different regions, first the surface layer which is heated daily by the sun and mixed by the winds. It is usually isothermal and also known as the mixed layer. Second layer is called the seasonal thermocline, wherein the temperature decreases with depth. During winter this may not exist due to the deep mixing of the surface layer. The permanent thermocline is the next layer which

is characterised by decreasing temperature and sound speed. The fourth region is the deep isothermal layer which is in the deep ocean which is not strictly isothermal but in which temperature only gradually decreases with depth. In this region sound speed increases as the depth increases due to increase in the pressure.

In the real ocean, the sound speed varies continuously with depth making prediction of acoustic ray propagation impossible except for simplified cases. However, by decomposing the sound speed profile by many small intervals or layers of constant sound speed and then reapplying Snell's law to sound traveling between layers, the ray path for arbitrary sound speed profiles can be approximated. This approach forms the basis of any ray tracing algorithm like the BELLHOP ray tracing algorithm [29][22].

In a medium which has a constant sound speed, the ray paths traveling as straight lines, indicate the propagation direction of a wavefront. When a sound wave traveling in a fluid medium encounters stratification, there is an abrupt change in density and sound speed, such as the air-water or water-seabed interface. The energy is reflected into the medium or transmitted through the medium. The following relationships for transmissions and reflections at interfaces are discussed in many texts [33] [22]. Considering a plane interface between two different media, with different sound velocities c_1 and c_2 as shown in Figure 2.2, the angle of refraction, θ_r is given by Equation 2.7.

For plane waves that arrive at an interface (See Figure 2.2), two boundary conditions will govern the solution for reflection, transmission, and refraction. Firstly, the pressures as a function of time on both sides of the interface must be equal. Therefore, $p_i + p_R = p_t$, where the subscripts, i , R and t correspond to the incident, reflected and transmitted pressures.

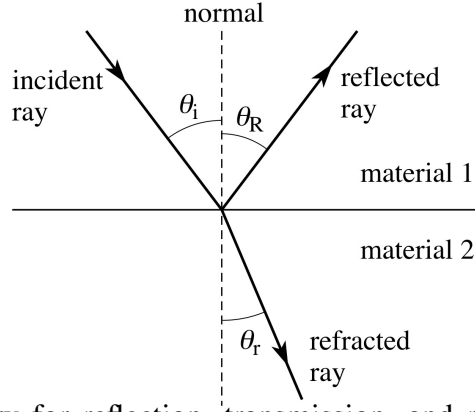


Figure 2.2: Geometry for reflection, transmission, and refraction of plane waves at an interface of two different material media.

The second boundary condition being that the components of velocity normal to the interface, as a function of time, are equal ($u_{yi} + u_{yR} = u_{yr}$). Here the x-axis is horizontal and z-axis is vertical on the page. Hence, the y-axis is perpendicular to the interface (into page). By solving the two boundary conditions, the coefficients for the transmitted (T_{12}) and reflected (R_{12}) waves are given by

$$R_{12} = \frac{\rho_2 c_2 \cos(\theta_i) - \rho_1 c_1 \cos(\theta_r)}{\rho_2 c_2 \cos(\theta_i) + \rho_1 c_1 \cos(\theta_r)} \quad (2.5)$$

$$T_{12} = \frac{2\rho_2 c_2 \cos(\theta_i)}{\rho_2 c_2 \cos(\theta_i) + \rho_1 c_1 \cos(\theta_r)} \quad (2.6)$$

where ρ_1 and c_1 are the density and sound speed in medium/material 1 and ρ_2 and c_2 are the density and sound speed in medium/material 2 as given in Figure 2.2. The transmitted wave propagation angle θ_r is given using Snell's Law according to

$$\theta_r = \arcsin \left[\left(\frac{c_2}{c_1} \sin(\theta_i) \right) \right] \quad (2.7)$$

Where θ_i is the incidence angle, θ_r is the refracted angle.

2.1.4 Attenuation

Attenuation in ocean waters is attributed mainly to the absorption by molecular and chemical relaxation. In the process of molecular relaxation, the amount of energy absorbed is related to the viscosity of the fluid. Chemical relaxation is the process of ionic dissociation and subsequent recombination with the passing of the pressure waves. In the ocean, pure water, boric acid, magnesium sulfate are responsible for most of the absorption [12]. Based on the laboratory and field data, an empirical equation accounting for the combined attenuation of sound by the three constituents was introduced by [10]. The attenuation equation split into terms for each of the three constituents, is

$$\alpha = \frac{A_1 P_1 f_1 f^2}{f^2 + f_1^2} + \frac{A_2 P_2 f_2 f^2}{f^2 + f_2^2} + A_3 P_3 f^2, \quad (2.8)$$

where the first, second and third terms account for absorption by boric acid, magnesium sulphate, and pure water respectively. The A coefficients contain empirical relationships that combine important variables that include salinity, sound speed, depth, temperature, pH of water and relaxation frequencies of the salts. P_1 , P_2 and P_3 are pressure dependencies and f_1 and f_2 are relaxation frequencies characteristic of the particular chemical process. Equation 2.8 suggests that the attenuation is highly dependent on frequencies. When all the constituents are combined, boric acid is important below 10 kHz, from 10 - 200 kHz magnesium sulphate dominates and above 200 kHz pure water is the most significant contributor.

2.1.5 Measurements of underwater sound

In order to measure underwater sound, we must convert the acoustic energy into electrical energy. An acoustic transducer is an electrical device that converts sound wave vibration or the pressure fluctuations into mechanical / electrical energy. A hydrophone is an underwater equivalent of the microphone. It consists of a piezoelectric sensor encased in a polymer shell with material properties that is closely matched to the acoustic impedance (ρc) of water (Refer Section 2.1.1 Equation 2.2). As the pressure waves pass through the piezoelectric sensor, a voltage is induced. This induced voltage can be used to measure the pressure.

Hydrophones are of two types, omnidirectional and directional. The omnidirectional one will detect sounds from all directions with equal sensitivity. The hydrophone receive sensitivity is usually given in decibels relative to 1 V per micropascal (dB re 1V/ μ Pa or dBV re 1 μ Pa). This unit is a measure of the voltage generated per unit of sound pressure in the fluid surrounding the hydrophone. The voltage is given relative to a reference voltage(V_0)equal to 1 V. The unit in decibels is given as in Equation 2.9.

$$20 \log \frac{V}{V_0} \quad \text{re 1V per } 1\mu\text{Pa} \quad (2.9)$$

where V is Voltage output of hydrophone per 1 μ Pa input pressure. The receive sensitivity is normally expressed in negative values. The term *Directivity* refers to directionality of the source or the receiving hydrophone. The Directivity Index (DI) is the ratio of the total noise power in an isotropic noise filled environment, incident on an array, compared to the power actually received by the system.

$$DI = 10 \log \frac{N_{\text{omni-directional noise}}}{N_{\text{directional noise}}} \quad (2.10)$$

Directional hydrophones have higher sensitivity to signals in a particular direction. The difference between the sound arrival times, reaching the hydrophone from different directions, can be used in calculations to determine the direction that the sound is coming from.

The receive sensitivity of a hydrophone is a curve as a function of frequency (see Figure 2.3). The value of the receive sensitivity of any hydrophone largely depends on the structure of the hydrophone. In case of spherical hydrophones, the larger the diameter of the hydrophone, the more sensitive will be the response but with a smaller frequency range. Hydrophones are usually used below their resonance frequency over a much wider frequency band where they provide uniform output levels. The positive peak in the receive sensitivity plot (Figure 2.3) occurs at resonance frequency. Resonance has to do with the size and the geometry of the piezo element. The hydrophone used in this document to record the underwater sound at both the sites on Grand Banks is enclosed within the recording system namely the AMAR (Autonomous Multichannel Acoustic Recorder), with receive sensitivity of -163.3 dB re $1\text{V} / \mu\text{Pa}$ at site DFO-CT and -164 dB re $1\text{V} / \mu\text{Pa}$ at site DFO-ST respectively. The plot of the hydrophone receive sensitivity response and the AMAR are shown in Figure 2.3 and Figure 2.4 respectively.

Figure 2.3: Receiver sensitivity graph of AMAR hydrophone

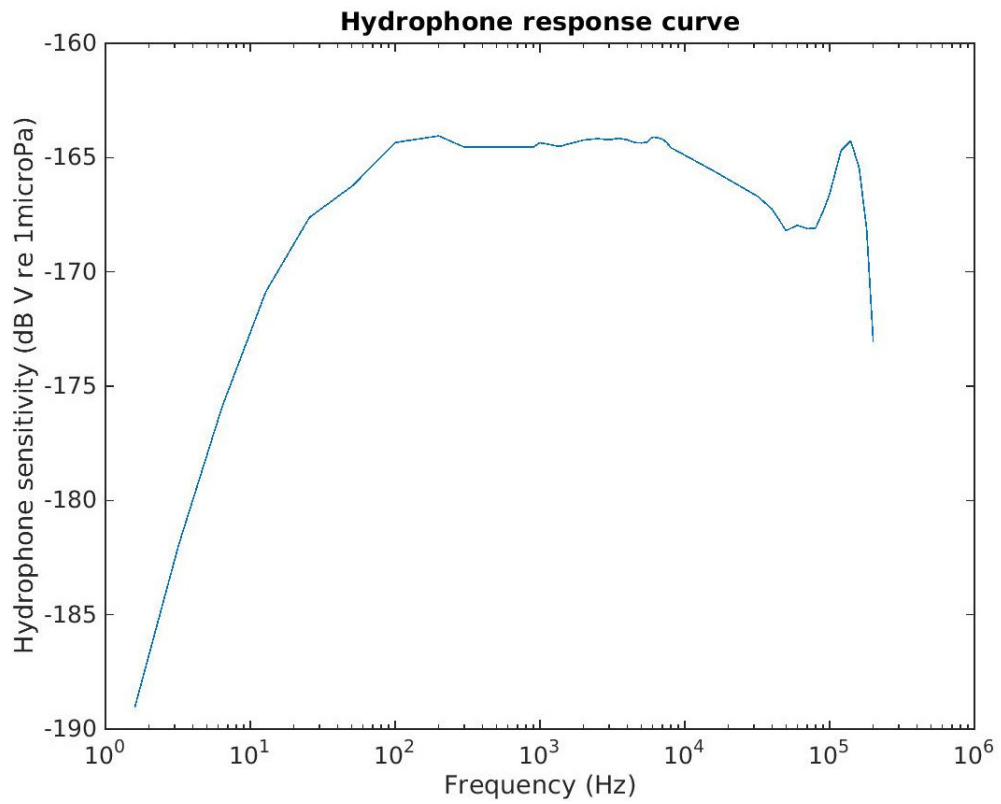


Figure 2.4: Autonomous Multichannel Acoustic Recorder

2.2 Signal processing

The analysis of sequential data is known as *time series analysis*. The basic purpose of the time series analysis method is to define the variability of a data series in terms of dominant

periodic functions. There are a number of common signal processing techniques that rely on the computation of the Fourier transforms to convert signals from the time domain to the frequency domain. The most commonly used signal processing technique is the Fast Fourier Transform (FFT) [8]. One of the prominent properties of a Fourier transform is the linear relationship between time series and the frequency spectrum i.e the total energy of the signal is conserved in the transformation.

2.2.1 Sampling theorem & DTFT (Discrete Time Fourier Transform)

The Sampling theorem establishes that for an accurate representation of a signal $x(t)$ by its time samples $x(nT)$ the signal must be band limited i.e its frequency spectrum must be limited to contain frequencies up to some maximum frequency, f_{max} . The sampling rate f_s must be chosen to be at least *twice* the maximum frequency, f_{max} as in Equation 2.11.

$$f_s \geq 2f_{max} \quad (2.11)$$

In terms of sampling interval,

$$T \leq \frac{1}{2f_{max}} \quad (2.12)$$

The *minimum* sampling rate allowed by the sampling theorem, i.e $f_s = 2f_{max}$ is called the *Nyquist rate*.

In order to understand the effects of sampling on using the Fourier transforms, the output of an analog signal $x(t)$, measured by a sampler instantaneously at instant $t = nT$ is considered to be an analog signal composed of the linear superposition of impulses occurring at sampling times, with each impulse weighted by the corresponding sample value. Thus

the sampled signal is given by Equation 2.13.

$$\hat{x}(t) = \sum_{n=-\infty}^{\infty} x(nT)\delta(t - nT) \quad (2.13)$$

Where $\delta(t - nT)$ is the dirac delta or the impulse function. The spectrum of the sampled signal $\hat{x}(t)$ is the Fourier transform given by Equation 2.14.

$$\hat{X}(f) = \int_{-\infty}^{\infty} \sum_{n=-\infty}^{\infty} x(nT)\delta(t - nT)e^{-2\pi jft} dt \quad (2.14)$$

$$= \sum_{n=-\infty}^{\infty} x(nT) \int_{-\infty}^{\infty} \delta(t - nT)e^{-2\pi jft} dt \quad (2.15)$$

$$\hat{X}(f) = \sum_{n=-\infty}^{\infty} x(nT)e^{-2\pi jfTn} \quad (2.16)$$

Equation 2.16 is known as the Discrete-Time Fourier Transform (DTFT)

2.2.2 Power spectral density (PSD)

It is well known that the energy in the time domain is equal to the energy in frequency domain as per Parseval's theorem. In other words, Parseval's theorem can be interpreted as the energy of a signal $x(t)$ is a result of energies contributed by all spectral components of signal $x(t)$.

Energy of a signal $x(t)$ is given as follows -

$$E = \int_{-\infty}^{\infty} x^2(t) dt \quad (2.17)$$

$$x(t) = \frac{1}{2\pi} \int_{-\infty}^{\infty} X(w)e^{jw t} dw \quad (2.18)$$

Substituting above equation in Equation 2.17, gives energy of signal as

$$E = \int_{-\infty}^{\infty} x^2(t) dt = \int_{-\infty}^{\infty} x(t) \left[\frac{1}{2\pi} \int_{-\infty}^{\infty} X(w) e^{j\omega t} d\omega \right] dt \quad (2.19)$$

$$E = \frac{1}{2\pi} \int_{-\infty}^{\infty} X(w) \left[\int_{-\infty}^{\infty} x(t) e^{j\omega t} dt \right] d\omega \quad (2.20)$$

since for real signal $X(w)X(-w) = |X(w)|^2$

$$E = \frac{1}{2\pi} \int_{-\infty}^{\infty} |X(w)|^2 d\omega = \int_{-\infty}^{\infty} |X(w)|^2 df = \int_{-\infty}^{\infty} \Psi(w) df \quad (2.21)$$

Hence $\Psi(w) = |X(w)|^2$ is called the *Energy Spectral Density* of the signal $x(t)$.

In case of periodic signals, the integral as given in Equation 2.17 is infinite and energy of such signals is no longer valid. In those cases, the time average of energy or the average power of signals is considered. Hence, such signals are *power signals*. In other words, signals that have infinite energy are called power signals. The average power of a signal $x(t)$ is given by Equation 2.22.

$$P = \lim_{T \rightarrow \infty} \frac{1}{T} \int_{-T/2}^{T/2} x^2(t) dt \quad (2.22)$$

The average power is also the mean square value of $x(t)$.

Let $x_T(t)$ be the truncated function of $x(t)$ during the interval $(-T/2, T/2)$, then

$$\int_{-\infty}^{\infty} x_T^2(t) dt = \frac{1}{2\pi} \int_{-\infty}^{\infty} |X_T(w)|^2 d\omega \quad (2.23)$$

but

$$\int_{-\infty}^{\infty} x_T^2(t) dt = \int_{-T/2}^{T/2} x^2(t) dt \quad (2.24)$$

Hence Average power is given as

$$P = \lim_{T \rightarrow \infty} \frac{1}{T} \int_{-T/2}^{T/2} x^2(t) dt = \frac{1}{2\pi} \int_{-\infty}^{\infty} \lim_{T \rightarrow \infty} \frac{1}{T} |X_T(w)|^2 d\omega \quad (2.25)$$

If

$$S_X(w) = \lim_{T \rightarrow \infty} \frac{1}{T} |X_T(w)|^2 \quad (2.26)$$

Then,

$$\text{AveragePower} = P = \frac{1}{2\pi} \int_{-\infty}^{\infty} S_X(w) dw = \int_{-\infty}^{\infty} S_X(f) df \quad (2.27)$$

Equation 2.27 represents total power of a signal which is the area under the curve of $S_X(w)$. Thus $S_X(w)$ represents power density per unit bandwidth. $S_X(f)$ is known as Power Spectral Density (PSD) as it represents how the power is distributed over the frequency range. PSD involves only information about the amplitude not the phase. The above discussed concepts can be simply summarized as follows: Power Spectral Density is the Power spectrum divided by Δf (displays power spectrum per unit frequency), where Δf is frequency resolution; Energy spectral density is power spectrum density times the data length i.e. Time (displays energy spectrum per unit frequency).

2.2.3 Welch's method

Welch's method, named after P.D. Welch is a spectral density estimation approach, used to estimate the power of a signal at various frequencies. This method is based on the concept of dividing the data into segments and allowing an overlap of these segments. Each data segment is windowed, prior to computing the periodogram. This method is also called the weighted overlapped segment averaging method or periodogram averaging method.

The following steps are involved in Welch's method -

- **Partition of the data sequence**

$$x[0], x[1], \dots, x[N-1]$$

into K segments or batches such that

segment 1:

$$x[0], x[1], \dots, x[M-1]$$

segment 2:

$$x[S], x[S+1], \dots, x[M+S-1]$$

.
. .
.

segment K :

$$x[N-M], x[N-M+1], \dots, x[N-1]$$

Where

M = Number of points in each segment

S = Number of points to shift between segments

K = Number of segments

- **Computing a windowed Discrete Fourier transform (DFT)**

For each segment ($k = 1$ to K), a windowed Discrete Fourier Transform (DFT) is

computed at some frequency $\nu = \frac{i}{M}$ with $-(\frac{M}{2} - 1) \leq i \leq \frac{M}{2}$:

$$X_k(\nu) = \sum_m x[m]w[m] \exp(-j2\pi\nu m)$$

where

$$m = (k-1)S, \dots, M + (k-1)S - 1$$

$w[m]$ = the window function

- **Forming the modified periodogram value**

For each segment ($k = 1$ to K), a modified periodogram value, $P_k(f)$ is formed from the Discrete Fourier Transform:

$$P_k(v) = \frac{1}{W} |X_k(v)|^2$$

where

$$W = \sum_{m=0}^M w^2[m]$$

- **Averaging the periodogram values**

Welch's estimate of the PSD can be obtained by averaging the periodogram values as below-

$$S_x(v) = \frac{1}{K} \sum_{k=1}^K P_k(v)$$

For any two adjacent segments in Welch's method, the number of points by which they overlap is given as $M - S$ or $100(\frac{M-S}{M})\%$. When $S = M$, there is no overlap between the segments. Whereas the segments contain 50% overlap when $S = 0.5M$.

2.3 Ambient noise

We are not the only living creatures on this planet. We need to live in harmony with other life forms. For us to survive, we need to make sure that we do not perturb the natural environment or disturb the balance of nature. A broad range of natural processes affect the underwater acoustic environment over a broad range of frequencies. There are different sources that dominate specific frequency bands.

Ambient or background noise levels are the product of many oceanic noise sources, including natural and distant man-made sources. Noise from natural sources is typically generated by physical or biological processes. Marine mammals heavily rely upon sound as a means of communication, for finding food & mates, and for detecting predators. Examples of physical processes generating noise are: tectonic (seismic) activity in the earth's crust (volcanoes and earthquakes), wind and waves, while examples of biological noise sources are the vocalizations of marine mammals and fish. The ambient noise levels in the earth's oceans have been increasing rapidly caused by global trade with increased shipping between different continents. Low frequency sound waves propagate over long ranges as they experience little attenuation. Noise from shipping activity is predominant at low frequency (< 300 Hz) and dominates the ambient noise levels throughout the ocean in the low frequencies [33].

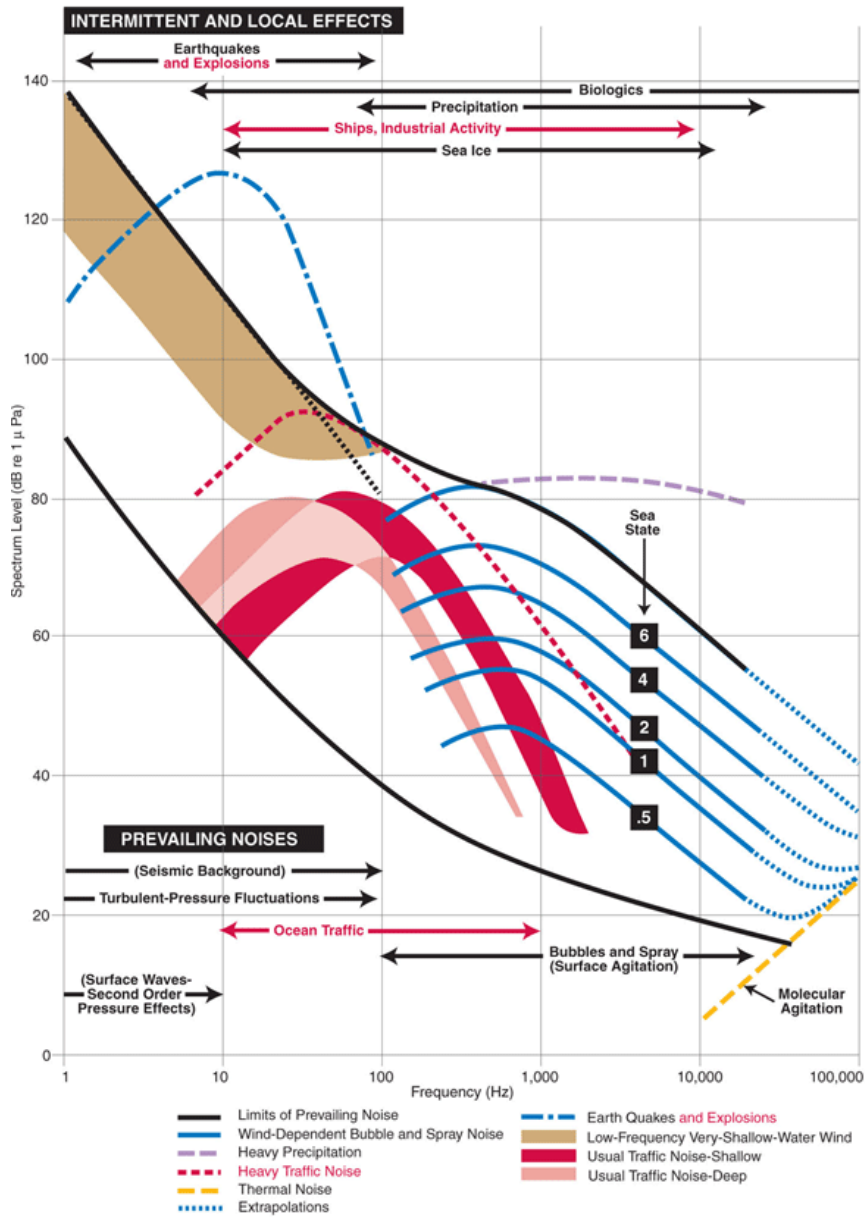


Figure 2.5: Wenz curves describing pressure spectral density levels of marine ambient noise from weather, wind, geologic activity, and commercial shipping for deep water conditions. (Adapted with permission from [7] [35])

The background noise in each marine area as shown in Figure 2.5 comprises of noise from different sources both near and far which differ seasonally and regionally for deep water areas. The received levels might differ in shallow water areas such as the current study sites, but these curves are a good approximation for the relevant contribution to each source contributing to the ambient noise. Spectral levels are plotted as function of frequency with the thick black lines indicating limit of prevailing ambient noise.

Sea criteria	Beaufort scale	Wind speed		12-h wind		Fully arisen sea		Sea-state scale
		Range knots (m/sec)	Mean knots (m/sec)	Wave height ^{a,b} ft (m)	Wave height ^{a,b} ft (m)	Duration ^{b,c} h	Fetch ^{b,c} naut. miles (km)	
Mirror-like	0	<1 (<0.5)						0
Ripples	1	1-3 (0.5-1.7)	2 (1.1)					1
Small wavelets	2	4-6 (1.8-3.3)	5 (2.5)	<1 (<0.30)	<1 (<0.30)			1
Large wavelets, scattered whitecaps	3	7-10 (3.4-5.4)	8½ (4.4)	1-2 (0.30-0.61)	1-2 (0.30-0.61)	<2.5	<10 (<19)	2
Small waves, frequent whitecaps	4	11-16 (5.5-8.4)	13½ (6.9)	2-5 (0.61-1.5)	2-6 (0.61-1.8)	2.5-6.5	10-40 (19-74)	3
Moderate waves, many whitecaps	5	17-21 (8.5-11.1)	19 (9.8)	5-8 (1.5-2.4)	6-10 (1.8-3.0)	6.5-11	40-100 (74-185)	4
Large waves, whitecaps everywhere, spray	6	22-27 (11.2-14.1)	24½ (12.6)	8-12 (2.4-3.7)	10-17 (3.0-5.2)	11-18	100-200 (185-370)	5
Heaped-up sea, blown spray, streaks	7	28-33 (14.2-17.2)	30½ (15.7)	12-17 (3.7-5.2)	17-26 (5.2-7.9)	18-29	200-400 (370-740)	6
Moderately high, long waves, spindrift	8	34-40 (17.3-20.8)	37 (19.0)	17-24 (5.2-7.3)	26-39 (7.9-11.9)	29-42	400-700 (740-1300)	7

^a The average height of the highest one-third of the waves (significant wave height).
^b Estimated from data given in U. S. Navy Hydrographic Office (Washington, D. C.) publications HO 604 (1951) and HO 603 (1955).
^c The minimum fetch and duration of the wind needed to generate a fully arisen sea.

Figure 2.6: Categories of sea state and wind speed and the effects to the Sea Surface.

(Adapted with permission from [35])

The condition of the sea surface is quantified by the Beaufort sea states, which is a number ranging from 0 – 8 as given in the Figure 2.6. Sea state is a unit describing

different wave heights (Example wind at Beaufort 4 = approx. sea state 3). The Beaufort wind scale, ranging from 0 – 12 is a standard measure of the consistent wind speed. The wind generated ambient noise contributions is directly proportional to the wind speed and the sea state.

2.3.1 Ship traffic

Low-frequency ambient noise in the open ocean have long been attributed to maritime traffic [35] [33]. Although we might not be able to differentiate between individual ships but altogether their noise is radiated in water and blends together to give a broadband humming noise. Dredging and other shore based activities too produce distinctive sounds. Since the higher frequencies typically get attenuated quickly, the lower frequency hum is the one that persists if sources were close enough. Low-frequency (< 500 Hz), high-energy (> 180 dB re $1 \mu\text{Pa}$) noise generated by large ships propagate very efficiently across the ocean basins contributing to ambient noise levels over large distances (> 100 Km) [7]. Whereas at shorter distances (< 10 Km), higher frequency noise may also be significant. The acoustic signature of a ship depends on its design characteristics like gross tonnage, draft, on-board equipment like generators, engines, etc and also on the operating conditions of the ship like speed and sea state [30]. The primary source for sound generation in the commercial shipping vessels as well as the naval vessels is the propeller cavitation. As the propeller rotates through the water, regions of low or negative pressure are created at its tips, if and when these negative pressures become sufficiently strong, bubbles (cavities) begin to form. These bubbles are short lived and collapse in either a turbulent stream or against the surface of the propeller. A sharp pulse of sound is produced as the bubble collapses and this

process, cavitation, is responsible for the loud hiss often associated with ships. Cavitation is a phenomenon of water vaporizing or "boiling" due to extreme reduction of pressure on the back of the propeller blades. Cavitation occurs on nearly all ship propellers, if it is not acknowledged at the early design stage of the propeller, leads to extensive problems like erosion on propeller blades, high frequency noise and vibration, etc. This process produces broadband noise and tonal components related to the rotation rate of the ship's propeller [11]. Radiated noise levels are also directional and vary based on the ship's orientation or aspect [4]

There are four main sound sources on a ship: a) Machinery that includes main propulsion and auxiliary machines. b) Propellers. c) Noise generated by the flow of water on the hull. d) Other noise generated within the ship especially under the water line. The volume and characteristics of noise generated by a ship will depend on the direction from where it is heard. Mostly due to the propeller, ships usually tend to radiate more noise to their stern than to the bow. Most of the machinery noise is concentrated at the precise frequencies above or at their harmonics thus called as tonal noise or narrow band noise and appears as narrow peaks in the spectra of ship's acoustical signature. Machinery noise also generates some broadband noise. Thus, close proximity to shipping lanes and harbors increases noise levels. Shipping traffic is one of the two dominant factors used to determine the ambient noise levels.

2.3.2 Biological sources

One of the primary sources of potential biological signal is the marine mammal vocalizations and echolocations. Many marine mammals intentionally produce sound for naviga-

tion purposes anywhere between very short duration pulses to whale songs. Marine mammal vocalizations occur over a wide range of frequencies [5]. Biological sound sources make a noticeable contribution at certain times of year. For example, a peak around 20 Hz created by calls of large baleen whales is often present in deep-ocean noise spectra. Groups of whistling and echolocating dolphins can raise the local noise level at the frequencies of their signals. Snapping shrimp are an important component of natural noise from a few kilohertz to above 100 kHz close to reefs and in rocky bottom regions in warm shallow waters. A variety of mysticete and odontocete species are known to occur in the Grand Banks. Many of these species are considered at risk as per the Government of Canada's *Species at Risk Act (SARA)* including endangered blue whales and the northern bottlenose whales, and the special concern fin whales, killer whales and harbour porpoise [31]. All marine mammals on the Grand Banks are known to be acoustically active. There are many species-unique calls which make them ideal candidates for passive acoustic monitoring.

2.3.3 Surface agitation

Surface agitation is mainly due to the interaction between ocean water and atmospheric wind. The sound produced by waves, spray and even water bubbles contribute to the ambient noise. The contribution of wind speed to the ambient noise is due to the breaking waves at the air-ocean interface caused primarily due to wind stress. The breaking waves consist of acoustically active bubbles which produce sound at frequencies dependent on the bubble diameter. The sound generated by wind has constant negative spectral slope of 20 dB / decade, that is independent of wind speed between 500 Hz to 20 kHz [20]. The higher the wind speed, the higher will be the level of sound produced by them.

Movement of water due to tides also contributes to the ambient noise levels. This movement can create large changes in ambient pressure in ocean. These changes will be most significant at very low frequencies (< 100 Hz) but will decrease in strength with increasing depth. Overall tides contribute very little to the ambient noise level.

2.3.4 Seismic activity

Regular seismic activities like earthquakes can affect acoustic spectra up to 100 Hz but are intermittent sources [35]. At any given time there is always a certain amount of low intensity level seismic activity occurring in the ocean bed [32]. Although major earthquakes or volcanoes are very rare to occur. As the sound propagates long distances in the ocean, the seismic activity can be heard anywhere.

2.3.5 Breaking of ice

The polar ice caps are always subjected to changes in temperatures which causes great amount of mechanical stress leading to cracking of ice. Cracks that occur in the ice vary in their length from millimeters to kilometers [17]. The hypothesis proposed for the ice breaking event is that whenever there is strong wind or currents, the ice will start to break at locations where the stress is greater[36]. The continuous breaking of ice and greater stress due to winds and currents will eventually generate more impulsive sound in the waters beneath the ice [36]. This cracking noise produces loud noise. Cracking of ice can increase the noise levels by as much as 30 dB. Marginal ice zone's interaction with ocean waves may increase the overall noise levels by 4 – 12 dB [9].

2.3.6 Rain

Rain induces considerable noise and contributes to the overall ambient noise in the waters [20]. It increases noise naturally occurring ambient noise levels by up to 35 dB across a broad range of frequencies spanning from several hundred Hz to greater than 20 kHz. Droplet sizes and wind speed do determine the effects of rainfall rates on the overall acoustic spectra. Noise generated as a result of light rainfall is highly dependent on the wind speed. The light rainfall is associated with generation of small droplets that produce sound basically via two mechanisms: the droplet impact thereby creates broadband noise followed by a louder resonating micro bubble. For drizzle present in light winds, a broad spectral peak of, 10 – 20 dB above the background can occur at about 15 kHz [26]. The constituent micro bubbles have a resonant frequency ranging from 12 to 21 kHz with average of 15 kHz [23].

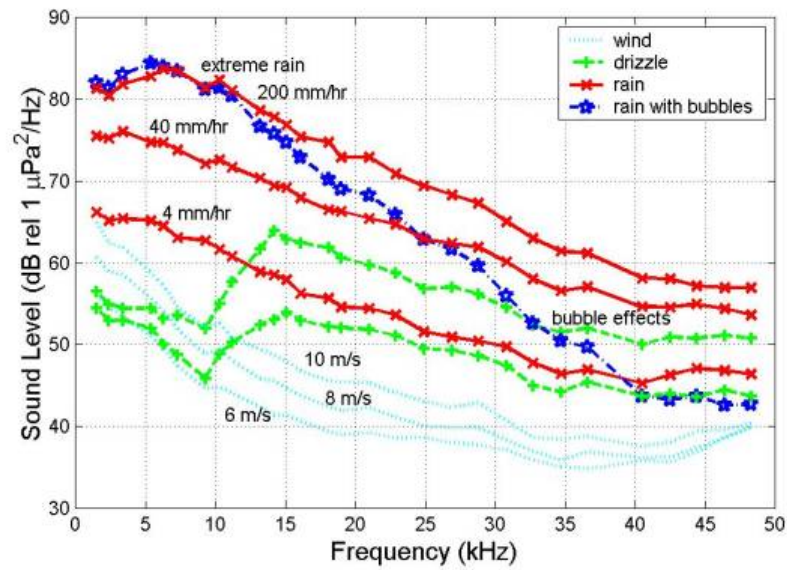


Figure 2.7: Examples of the spectral signals for different geophysical sound sources observed from the data from an ocean surface mooring in the South China Sea. (Adapted with permission from [20])

Wind generated sound has a very unique shape when compared to that generated by rain. Figure 2.7, shows the examples of various spectral signals for different geophysical sound sources observed from the data from an ocean surface mooring in the South China Sea. There is a distinctive peak due to drizzle for the spectrum between 12 - 25 kHz whereas the extreme rain sound results in large increases in sound levels over a wide frequency range. The effects of rainfall rates on the overall ambient noise acoustic spectra depend upon the droplet sizes as well as the wind speed.

2.3.7 Shallow and deep water ambient noise

Largely based on the nature of sound propagation from sources that are located near the sea surface, there is a huge dichotomy between shallow and deep water ambient noise [14]. Knudsen summarized in his work done before 1945 that the ambient sea noise is primarily dependent upon the interaction between sea state and wind force in the absence of any man-made and biological noises. The Knudsen curves relate wind force and sea state to the spectrum levels of ambient noise within the 100 Hz -20 kHz range [28]. A very detailed description of ambient noise is given by [35] and also in a publication by [2] that do discuss some of the changes and trends that occurred in the past 40 years.

Wenz compared the pressure spectra from many sources in the frequency band 1 cps to 20 kc (cps = cycles per second) and attributed several sources of noise contributing to the ambient noise levels.

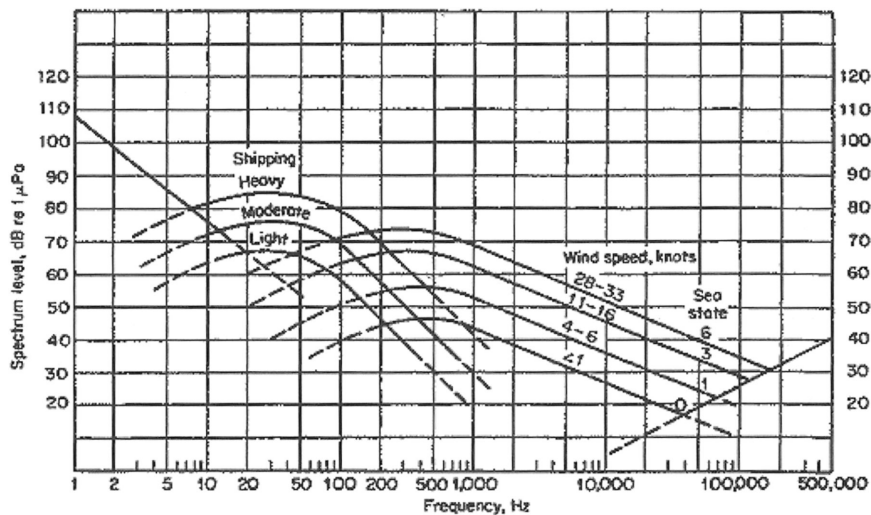


Figure 2.8: The average deep water ambient noise spectra. (Adapted with permission from [33])

Figure 2.8 gives a description of the different conditions of shipping and windspeed [33]. The heavy shipping curve is used for locations near the shipping lanes of the North Atlantic and the light shipping curve is appropriate for locations remote from ship traffic. Ambient noise varies with azimuth and vertical angle of arrival.

2.3.8 Ambient noise levels as a function of depth

Deep water ambient noise is largely dependent upon the nature of sound propagation from sources located near the sea surface. The deep water has an environment where there is almost no bottom interaction of sound from distant sources (generally speaking of the commercial shipping). Wenz noted that the ambient noise levels in deep water are lower by 5 dB than the shallow water noise levels at the same wind speed and frequency. Subsequent work done researchers indicate that shallow water levels show some wind speed dependence at all frequencies while deep water levels show almost no such dependence [3]. They concluded that shallow water noise is higher at all frequencies when compared to deep water. Subsequent work done for a 30 day period at deep ocean site off Bermuda with hydrophone at depth of 4.38 km, researchers came up with reasonable agreement of ambient noise levels with that obtained by Wenz and Knudsen *et al* [28]. Wind generated fluctuations dominated the spectra between 112 Hz - 2816 Hz while distant shipping dominated spectrum at frequencies between 17 Hz - 112 Hz. Depth-dependence of wind-driven broadband ambient noise in the Philippine Sea was carried out using Deep sound measurement system with the hydrophone being deployed at a depth of 6000 m but with varying depth as the two hydrophones ascend and descend to produce some interesting features of ambient noise unlike the previous investigations done at fixed depths [6]. In the frequency

band, 1 to 10 kHz, all the observed noise is downward travelling, signifying that bottom reflections make a negligible contribution to the ambient noise field, even at depths in the proximity of the seabed [6].

Chapter 3

Nystuen weather classification

3.1 Introduction

In this chapter, Nystuen's weather classification algorithm is discussed which is an algorithm used to identify various sources of sound like wind, rain, drizzle and shipping. Different underwater sound sources have different spectral shapes. These differences allow the algorithm to determine which process is dominating the sound field at a given point of time. Knowledge of sound sources is used to understand the source level that is making the noise underwater.

3.2 Algorithm for weather classification

The Nystuen weather detection algorithm [25] scales for four distinct conditions:

- Shipping and other contamination
- Heavy rain

- Wind with drizzle
- Bubbles present

The algorithm relies on spectral shape differences to identify the above listed sound sources. In addition to the weather conditions, shipping is a significant ocean noise source that in the present context must be detected in order to eliminate contamination. The check for detecting shipping noise and other contamination in the low frequencies is based on the fact that there are higher levels of low frequency sound contributed by shipping relative to the high frequency sound. Hence, when such conditions are found, it is assumed that shipping or other man made noise is the dominant contributor [18].

3.2.1 Check for excess low frequency sound

Shipping is a major contributor to the underwater ambient sound especially at low frequency. It is detected by comparing the sound power at 4 kHz with the level at 20 kHz. If shipping noise is present, then the sound power at 4 kHz will be anomalously high. This condition is found by plotting the sound level at 20 kHz against the 4 kHz level (See Figure 3.1). In this representation, shipping contamination is identified by outlying points.

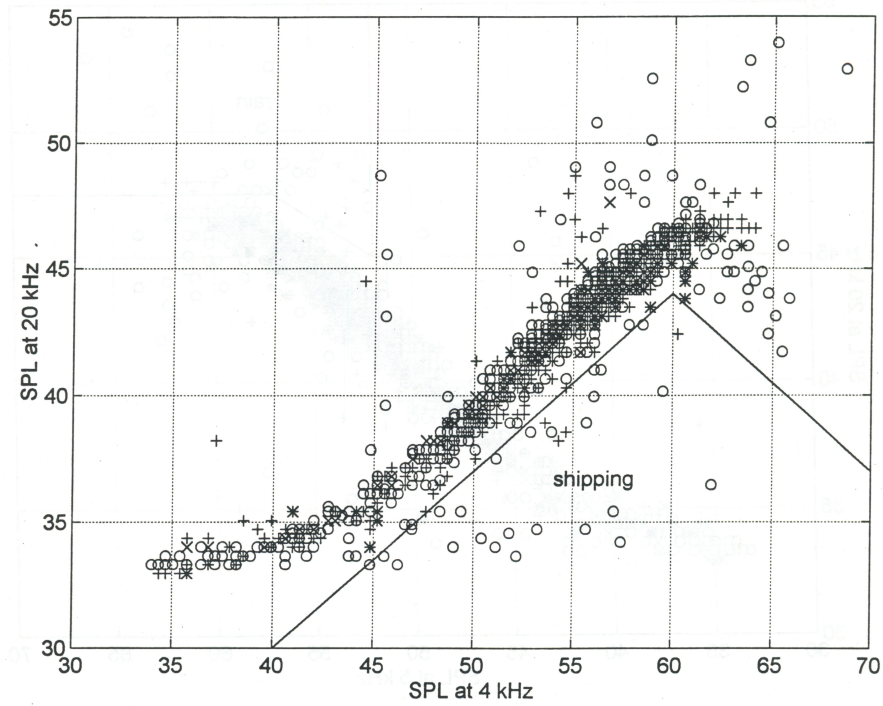


Figure 3.1: 20 kHz sound Vs. 4 kHz sound levels. (Adapted with permission from [25])

Shipping noise is identified by that region of the plot with anomalously high low frequency noise. The shipping noise detection is quantified as:

$$SPL_{20000} < (0.7) SPL_{4000} + 2$$

and

$$SPL_{20000} < (-0.7) SPL_{4000} + 86 \tag{3.1}$$

3.2.2 Check for high frequency sound - heavy rain

At very high frequencies of above 20 kHz, heavy rain produces very high sound intensity. Detection of heavy rain relies on these high frequency sound levels. There are two tests that can be done on the data set to check for this high frequency sound associated with heavy rain. We check for high levels of sound at 20 kHz compared to that at 5 kHz (See Figure 3.2).

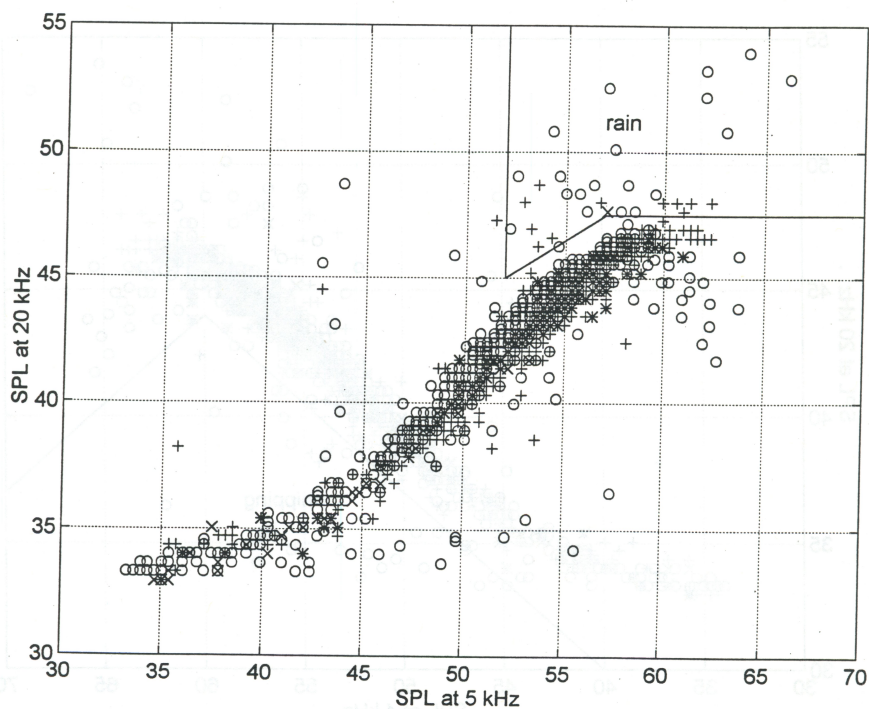


Figure 3.2: Rain detection test using 5 kHz and 20 kHz. (Adapted with permission from [25])

The vertical line seen in Figure 3.2 at around 52 dB separating rain from drizzle is present because the rainfall rate algorithm [27] is valid only for sound levels above 52 dB.

In the presence of heavy rain, sound levels at about 20 kHz are suppressed by ambient bubbles, hence there is a second condition used to check for heavy rain as given by Equation 3.3.

3.2.2.1 Test 1 - Heavy rain

This condition checks for heavy rain by comparing the sound pressure levels at 20 kHz and 5 kHz.

$$\begin{aligned}
 SPL_{20000} > 47.5 \quad \text{or} \quad SPL_{20000} > (0.5)SPL_{5000} + 19 \\
 & \hspace{15em} \text{and} \\
 SPL_{5000} > 52 \text{ dB} \hspace{10em} (3.2)
 \end{aligned}$$

3.2.2.2 Test 2 - Heavy rain

The need for Test 2 arises due to the fact that the Test 1 often times fails to detect heavy rain when there are bubbles present in the ocean, that suppress the sound levels, at around 20 kHz. This test detects heavy rain in presence of bubbles.

$$SPL_{20000} + (1.1)SPL_{8000} > 109.5 \text{ dB} \hspace{5em} (3.3)$$

The rainfall rate algorithm [27] can then be applied to the data point after performing the above Test 2.

The algorithm is given by

$$\log_{10}R = \frac{SPL_{5000} - 51.9}{10.6} \quad (3.4)$$

where R is the rainfall rate given in mm/hr. There is no processing of the data further since heavy rain conceals the sound thus generated by every other processes especially the wind associated sound.

3.2.3 Check for drizzle

The mechanism of sound production involving small raindrops (1mm diameter) is known to increase sound levels starting from 13 kHz upto about 20 kHz. These small raindrops also called drizzle do not affect the frequencies less than 13 kHz, hence in theory, the wind speed measurement is fairly good in the presence of drizzle. At about the sound level at 8 kHz, where the acoustic wind speed algorithm is applied [34], this drizzle turning into rain affects the wind speed as it tends to contaminate it by the rain noise. The drizzle test (as shown in Figure 3.3) uses the SPL at frequencies 8 kHz and 20 kHz to identify the data points contributing to the drizzle in the presence of wind (see Figure 3.3).

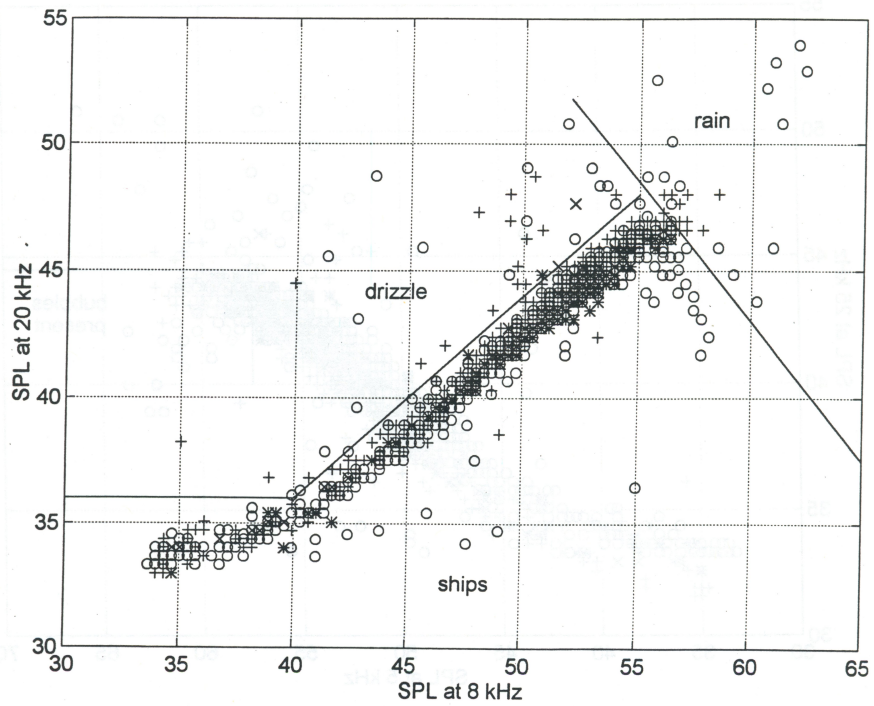


Figure 3.3: Drizzle detection test using 8 kHz and 20 kHz. (Adapted with permission from [25])

The condition of drizzle is detected in data when:

$$SPL_{20000} > (0.8)SPL_{8000} + 4 \quad \text{and} \quad SPL_{20000} > 36dB \quad (3.5)$$

If the above condition is met, then the data point is flagged as drizzle and can be further processed to measure wind speed.

3.2.4 Check for bubbles present

Bubble layers are formed in the oceans due to extensive wave breaking that occurs at wind speeds exceeding 10 m/s. These layers are an ensemble of plumes and clouds, the effect of which on the sound field is the change in the acoustic spectrum [18]. At their resonant frequencies, the bubbles absorb and radiate sound very efficiently. Within an actively breaking wave, the newly created bubbles radiate sound. Above 10 kHz, the slope of the spectrum becomes very steep, more than -25 dB / decade. The steepness arises because the bubbles preferentially attenuate the high frequency sound intensities, whereas the lower frequencies (< 5000 Hz) are not affected. It is the size of the bubbles which influence the sound frequency. The small bubbles really impact higher frequency sound but their response is less significant at lower frequencies. Hence the test for *bubbles present* uses 5 kHz and 25 kHz as can be seen in Figure 3.4.

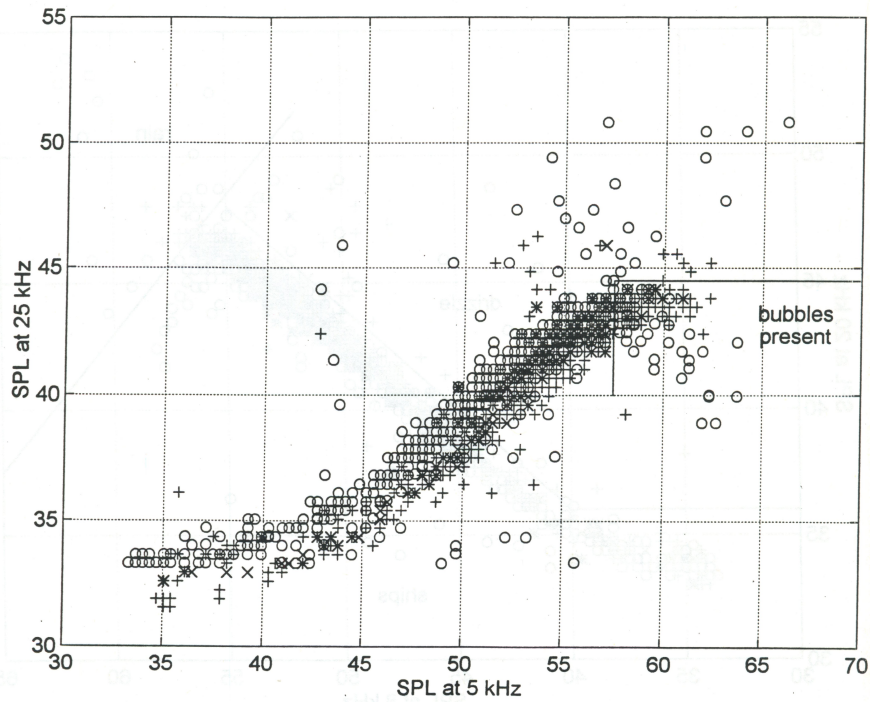


Figure 3.4: Bubble detection test using 5 kHz and 25 kHz. (Adapted with permission from [25])

If the condition given by Equation 3.6 is met, then the ambient bubbles are detected.

$$SPL_{5000} > 58 \text{ dB} \text{ and } SPL_{25000} < 44.5 \text{ dB} \quad (3.6)$$

3.2.5 Wind speed algorithm

The wind speed algorithm was first given by [34]. This algorithm is valid only for wind speeds from 2 – 15 m/s \pm 2 m/s. For wind speeds below 2 m/s, there is no wavelet or wave breaking that occurs, hence no generation of wind produced sound in the water. This

algorithm was developed using wind speeds of less than 15 m/s and may still be valid above 15 m/s, but with an unknown error.

The Wind speed algorithm is given by Equation 3.7:

$$U_{10} = \frac{10^{SPL_{8000}/20} + 104.5}{53.91} \quad (3.7)$$

where U_{10} is the 10 – meter wind speed in m/s.

Chapter 4

Bottom interaction model

4.1 Introduction

Ambient sound in the ocean can be used to estimate the wind speeds in the deep ocean. The rainfall rates may also be extracted from these signals. The low frequencies dominate the spectrum of ambient sound with the sound levels decreasing at a rate of approximately 20 dB/decade. Due to wave breaking in the ocean, bubbles are injected into the ocean surface associating wind with the ambient sound [21]. In fact, it has been established that the sound generated by a single breaking wave is proportional to the lost energy by the wave [24]. Melville et al.'s result is significant because it links up the ambient sound generated by wind to the dissipated energy by wind stress rather than wind itself. In shallow water, signal levels are altered by the occurrence of bottom reflections and these changes introduce errors in the rainfall and wind speed extraction algorithms. This chapter explores a simple analytical model to quantify these potential sources of signal contamination.

In Figure 4.1, the receiver is located at a depth D , the origin is located at the surface

directly above the receiver, r and ϕ are the polar coordinates in the surface plane used to identify uniformly distributed source elements having a dipole source characteristic ($I(R, \theta) = a^2 \cos^2(\theta) / R^2$).

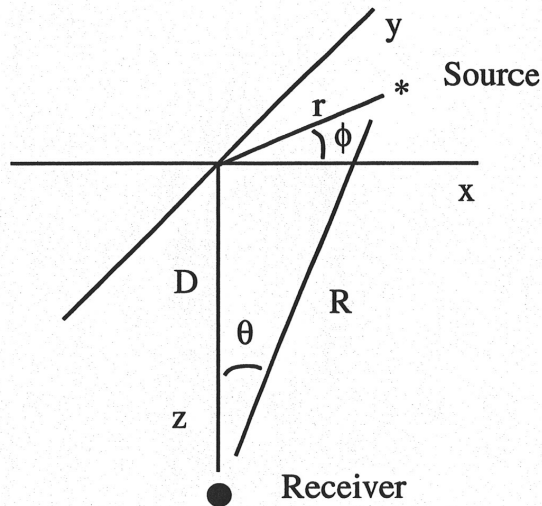


Figure 4.1: Basic model of surface generated sound

The surface and bottom reflections are modeled using the concept of images sources (see Figure 4.2). The source of sound has a dipole characteristic [1] although one might expect it to be omnidirectional as it's an oscillating air bubble. The presence of an image source across the ocean surface is what creates the dipole, which projects the acoustic energy downwards. Sound generation for typical oceanic conditions occurs whenever there is wave breaking, leading to a distribution of incoherent sources over the entire ocean surface. Ocean being a non perfect medium, the chemical absorption of sound by the sea

water tends to attenuate the higher frequencies. The sound power levels do not fall off with increasing depth of water for such a source, thus allowing for observations of sound levels at greater depths (see for example [16]). Several studies done by [18], [34], [16], have provided much insight into the working relationships between ambient sound and the wind speeds. The general form of the relationship between mean signal levels and wind speeds is well established, the understanding of the spectrum to a fuller extent remains unexplored. The -20 dB/decade has been consistently reported as the overall slope of the ambient sound spectrum. The slope has been demonstrated to be a consequence of the different bubble size distributions [21] [34].

4.2 Surface and bottom interactions

In the deep ocean, it is reasonable to model the ambient sound as that being generated at a plane surface on an infinite half space [34]. Whereas in shallow water this approach is not suitable due to the presence of bottom reflections. Bottom reflections when present, seem to enhance the overall observed ambient sound levels [18].

Using the concept of image sources, the effects of bottom reflected sound can be modeled with the assumption of only specular reflections [13] [18] as well as determination of the spectral form and levels affected by bottom reflections. As sound is being generated by all the points on the surface, the listening area has a radius that is comparable to the instrument depth [34]). The source underneath the surface acts as a dipole, instead of reflecting sound in all directions, it reflects in one direction. The presence of the ocean surface close to the oscillating bubble is what creates a dipole characteristic.

The geometry of the model is indicated in Figure 4.1. Consider a point receiver at some

depth D , with an infinite plane horizontal surface and bottom, in a homogeneous ocean. Along the surface, the acoustic sources are considered to be uniformly distributed having a dipole characteristic (consistent with the model of [34] and [16]). The sound level I , at a depth D is determined by integrating over the ocean surface as

$$I = \int_{\phi=0}^{2\pi} \int_{r=0}^{\infty} \frac{a^2}{R^2} \cos^2 \theta e^{-2\alpha R} r \, dr \, d\phi \quad (4.1)$$

where a is the spatial source level density, r and ϕ are the polar coordinates for the origin at a point on the surface directly above the receiver, R is the receiver distance from the source, θ is the angle between the dipole axis and the vertical made by a line joining the source and the receiver. The term $e^{-2\alpha R}$ has been added to express the chemical absorption of sound where α denotes the frequency dependent absorption in nepers/meter. Using the relation $\cos \theta = \frac{D}{R}$ and integrating over ϕ , Equation 4.1 can be expressed as

$$I = \int_{r=0}^{\infty} \frac{2\pi a^2 r D^2}{R^4} e^{-2\alpha R} \, dr \quad (4.2)$$

It is more convenient to convert the integration in Equation 4.2 from r to an integration over the angle θ . Making this conversion, Equation 4.2 becomes,

$$I = 2\pi a^2 \int_0^{\frac{\pi}{2}} \cos^3 \theta \sin \theta e^{\frac{-2\alpha D}{\cos \theta}} \, d\theta \quad (4.3)$$

Both the surface as well as the bottom are considered to be acoustic mirrors (with some loss), hence successive multiple reflections appear as virtual sources to the receiver. Using this concept, each order of reflection appears as a virtual surface at an adjusted depth

with source levels attenuated according to the number of surface and bottom interactions undergone. The geometry of the first two image planes is shown in Figure 4.2;

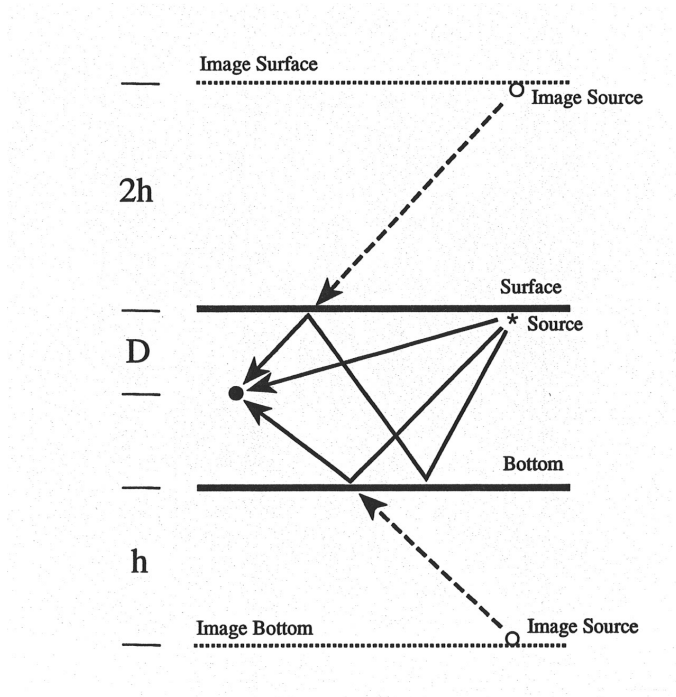


Figure 4.2: Geometry of image sources used in modeling multiple surface and bottom reflected rays

where the single bottom bounce ray creates an image plane at an equivalent depth of $-(2h - D)$, the bottom surface bounce ray creates an image plane at an equivalent depth of $2h + D$. The successive higher order image sources are added with appropriate adjusted depths. If β denotes the fraction of the acoustic energy that the bottom interactions absorb and γ denotes that for surface reflections, then the addition of bottom/surface reflections into Equation 4.3 leads to Equation 4.4.

$$I = 2 \pi a^2 \int_0^{\frac{\pi}{2}} \cos^3 \theta \sin \theta \left(e^{\frac{-2\alpha D}{\cos \theta}} + \beta e^{\frac{-2\alpha(2h-D)}{\cos \theta}} + \beta \gamma e^{\frac{-2\alpha(2h+D)}{\cos \theta}} + \dots \right) d\theta \quad (4.4)$$

where h denotes the water depth. The infinite sums in Equation 4.4 are a geometric series in exponential terms. Thus, Equation 4.4 can be expressed as,

$$I = 2 \pi a^2 \int_0^{\frac{\pi}{2}} \cos^3 \theta \sin \theta \left(\left(\frac{e^{\frac{4\alpha h}{\cos \theta}}}{\beta \gamma} - 1 \right)^{-1} \left(e^{\frac{-2\alpha D}{\cos \theta}} + \frac{1}{\gamma} e^{\frac{2\alpha D}{\cos \theta}} \right) + e^{\frac{-2\alpha D}{\cos \theta}} \right) d\theta \quad (4.5)$$

4.3 Summary

This basic model places a receiver at some depth in an ocean with an infinite plane surface and bottom. The sound speed gradients are not considered in the model and so sound cannot be channeled. Both the surface and bottom reflections are assumed to be purely specular and treated as forming mirror images of the surface sources. The absorption associated with both surface and bottom reflections is accounted for with a frequency independent reflection coefficient. A value of $\gamma = 1$ is chosen for all cases, as the surface reflection coefficient. The selection of this value assumes that the losses at the surface will be small and that while sound scattering will take place, there will be no loss of acoustic energy through this mechanism [19]. For the bottom reflection coefficient values of between -4 and -10 dB are considered consistent with field measurements of this parameter [33]. The various effects represented by Equation 4.5 are considered in isolation so that their collective response can be easily obtained from their individual contributions. In order to do this, the bottom is removed by selecting an infinite depth, thus isolating the effect of receiver depth on the received signal.

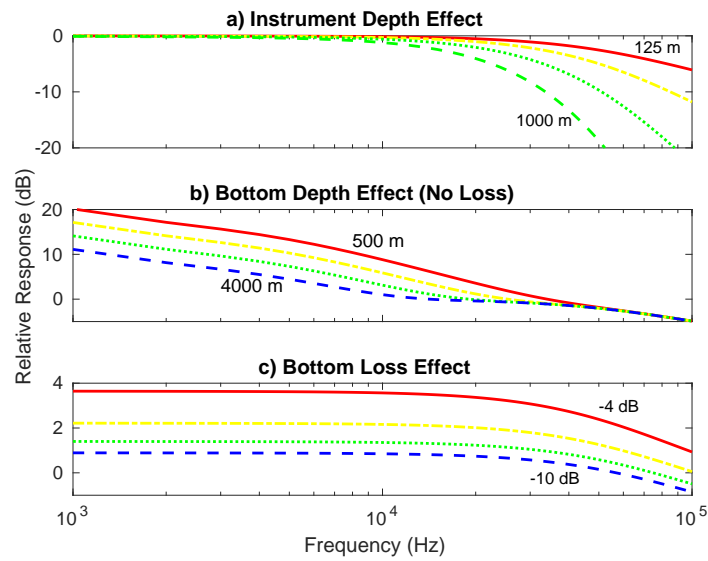


Figure 4.3: Effects of instrument placement, and bottom characteristics on received signal. Response is indicated in dB relative to source levels at the surface. a) No bottom reflections, only the effects of acoustic absorption are considered, depths of 125 m, 250 m, 500 m and 1000 m are shown. b) Bottom effect; examples of how the received signal at a depth of 100 m is altered by the presence of a (0 dB loss) bottom at depths of 500 m to 4000 m. c) Bottom effects; receiver is positioned on the bottom at a depth of 30 m, bottom attenuations of -4 dB, -6 dB, -8 dB and -10 dB are shown.

Figure 4.3(a) shows the effect of frequency dependence of the absorption term α on reducing the sound levels at higher frequencies. Frequency is indicated on the x axis for all the sub plots within Figure 4.3. Figure 4.3(b) shows the effect when bottom reflections are added (with no attenuation), there is an increase in the received signal level. It shows the received spectra predicted for a sample depth of 100 m and varying the bottom depths ranging from 117.3 m (this depth was selected to match the present field data), 1000

m, 2000 m and 4000 m. The changes to spectrum are only a consequence of acoustic absorption acting over greater propagation distances, with no bottom loss considered in this trial.

The effect of bottom loss is investigated by placing the receiver on the bottom in a shallow (30 m deep) sea and altering the reflection coefficient at the bottom. Figure 4.3(c) displays the received levels dependent of frequency for a variety of bottom reflection coefficients. An important consideration in this model is that the bottom interaction effect is independent of frequency and that the frequency dependence is due to acoustic absorption and the total distance travelled by the received signal. As is expected, it can be seen in Figure 4.3(c), an increase in the signal level associated with decreasing bottom loss coefficients. With a bottom loss of -4 dB, the signal level increases by 4 dB, while for a bottom loss of -10 dB the signal level increases by 1 dB.

When the bottom is removed to some intermediate depth below the instrument, Equation 4.5 predicts the response due to the combined action of the receiver depth and the bottom reflections. Figure 4.4 shows an example of such a response for an instrument placed at 100 m depth over bottom depths ranging from 500 m to 4000 m using a bottom loss coefficient of -5 dB.

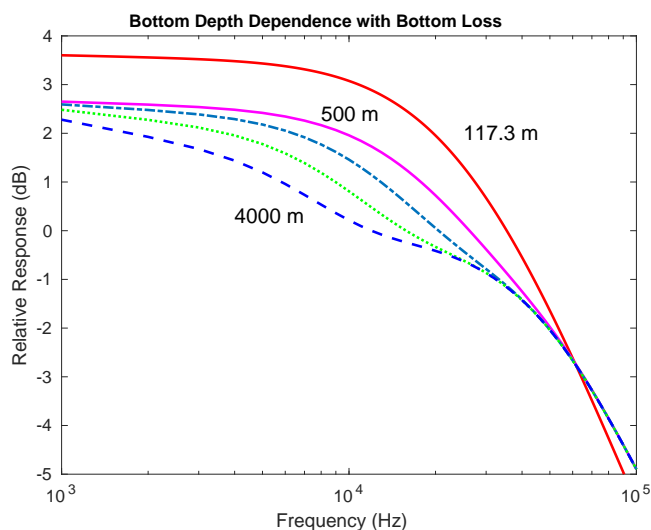


Figure 4.4: Spectrum of received sound at 100 m depth as caused by (white) surface generated ambient sound

At high frequencies (say above 40 kHz) the bottom depth is unimportant: the received signal is dominated by ray paths direct from the surface. At the lowest frequencies considered, the difference in response between different bottom depths again becomes small because chemical absorption at these frequencies is small. The middle regions (of between 3 kHz to 40 kHz) is the most complicated because of the interplay between chemical absorption and bottom reflected contributions. At the lower frequencies, increases in received levels of almost 3 dB can be realized. The model suggests that even in relatively deep water (4000 m) source levels can be increased by more than 1 dB, at frequencies below 5 kHz.

More important than the overall enhancement of signal levels due to bottom interactions is the frequency dependent slope that can result. Consideration of Figure 4.4 shows that a slope in the response spectrum of between 2 and 4 dB/decade can result because of bottom reflection and chemical absorption. Ambient sound observations report spectral slopes in

the range from -17 to -20 dB/decade. From the predictions of Equation 4.5, such variability may be the result of bottom reflected contributions at the various sample sites.

The interaction of low frequency enhancement (through reflections) and high frequency suppression through absorption have the effect of altering the spectral slope of the observed spectrum. For practical ocean depths and deployment geometries, signals at about 10 kHz appear to have a balance between reflection enhancements, and absorption losses. We therefore conclude that low frequency signal is strongly enhanced in using the bottom interaction model and there is a significant reflection loss probably occurring in practice hence the results from this model have been explored for the current study of this thesis.

Chapter 5

Data methods and results

5.1 Data acquisition

One of the most economically and ecologically valuable species found in Atlantic Canada (<http://www.dfo-mpo.gc.ca/>) are the Snow Crabs (*Chionoecetes Opilio*). A very large number of these crabs are found in the waters off Newfoundland & Labrador in the shelf area. A project, to understand the Soundscape characterization as well as the marine mammal presence on the Eastern Grand Banks, was initiated by Department of Fisheries & Oceans (DFO) to understand the effects of seismic exploration on the Snow Crabs. In support of this research, JASCO Applied Sciences (JASCO) partnered with DFO to investigate the ambient soundscape at a site where the seismic effects on Snow Crabs will be tested and sound levels predicted from a planned seismic exposure. Our interest in this project was to establish the baseline underwater sound levels and identify the natural variations contributed by rain, wind and drizzle and compare the wind speeds (obtained based on Nystuen wind algorithm) with that obtained from the wind model provided by Department of Fisheries

and Oceans (DFO) Newfoundland for the region of study.

As part of this project, two underwater acoustic recorders were deployed at a Grand Banks sites for a 46 and 48 day duration, respectively (Table 5.1, Figure 5.1). The first recorder was deployed at the study site called Station DFO-ST and the other one at the control site called Station DFO-CT. These locations are 72.34 kilometers apart. Autonomous Multichannel Acoustic Recorders (AMARs) have been used to record the underwater sound at the mentioned sites. Each AMAR was fitted with an M36 omnidirectional hydrophone (GeoSpectrum Technologies Inc.) and the hydrophone is protected by a cage, covered with a shroud to reduce the noise artifacts caused by the water flow above it. The AMAR hydrophones recorded on a duty cycle of 64 kHz sampling frequency (64 000 samples per second) for a bandwidth recording of 10 Hz to 32 kHz for a duration of 7 minutes followed by 375 kHz sampling frequency (375 000 samples per second) for a bandwidth recording of 10 Hz to 187 kHz for a duration of 1 minute. The recording channel had a 24-bit as well as a 16-bit resolution and sound was recorded on both these channels.

5.1.1 PGS survey track

A PGS (Petroleum Geo-Services) vessel, *Atlantic Explorer*, conducted a 2-D seismic survey in a wide area of the edge of Grand Banks in 2015. The survey ran from 4 Jul to 24 Oct 2015. The Closest Point of Approach (CPA) to the station DFO-ST was 1460 m on 28 Sept 2015; the CPA to the control site (DFO-CT) was 46177 m on 19 Sept 2015. The AMARs (acoustic recorders) were not equipped to measure the high level signals from the survey, so they were saturated when the vessel was ~8 km away in deep water or 16 km away in shallow water.

Table 5.1: Deployment and retrieval dates along with locations for the AMARs

Station	Deployment	Recovery date	Latitude (⁰ N)	Longitude (⁰ W)	Water depth(m)	Recorder depth(m)
DFO-CT	24 Aug 2015	11 Oct 2015	44 ⁰ 54'	-49 ⁰ 16'	179	155
DFO-ST	24 Aug 2015	09 Oct 2015	45 ⁰ 26'	-48 ⁰ 45'	243	117

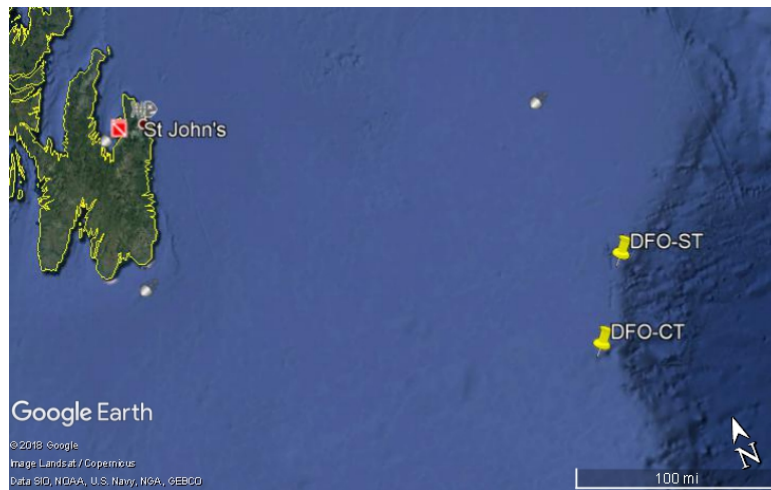


Figure 5.1: Map showing locations of AMAR stations DFO-CT and DFO-ST

Figure 5.2 shows the AMAR in-line mooring with a dual acoustic release assembly. The mooring was deployed via a free-fall from the surface of water at the two locations.

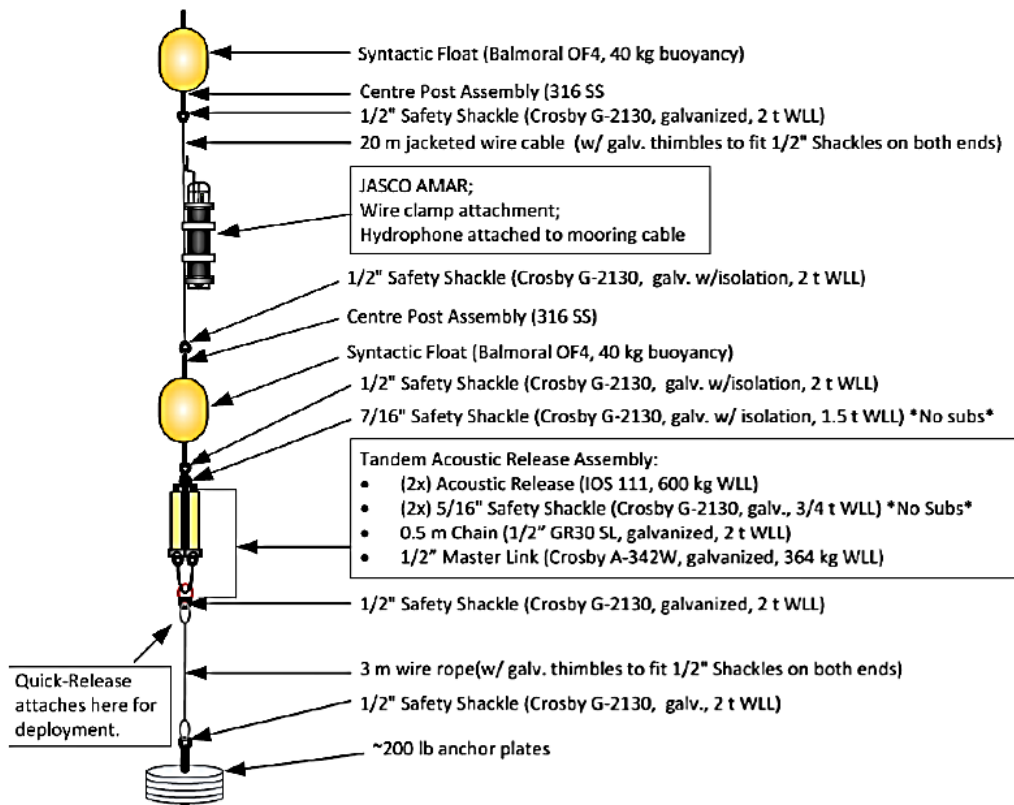


Figure 5.2: AMAR in-line mooring diagram

5.2 Analysis and results

All recordings for the stated periods of time consisted of about 17,000 WAV (Waveform audio file) - formatted files totaling to about more than 1.7 TB of data. Data was processed in MATLAB (version 2014b) using m-files to build the codes necessary to analyze the WAV files.

In order to understand the signal structure, the frequency content of the signals must be analysed. This analysis requires conversion to frequency representation from the time

domain using a Fourier transform. Thus, maximum frequency component for a signal sampled at 64 kHz (sampling frequency) is 32 kHz (sampling frequency / 2) and that at 375 kHz would be 187 kHz.

Figure 5.3 shows the advantage of performing Power Spectral Density (PSD) when compared to unaveraged power spectrum. Welch's method was used as an estimator of the PSD (Refer to Section 2.2.3 of Chapter 1). The averaging of the modified periodograms tends to decrease the variance of the estimate relative to a single periodogram estimate of the entire data set. Figure 5.3 is output of one .wav file from site DFO-CT at sampling frequency 64 kHz representing 7 minutes of data. The figure was generated by using *pwelch* function in MATLAB with an *nfft* value of 4096 and a 50 % overlap of the segments.

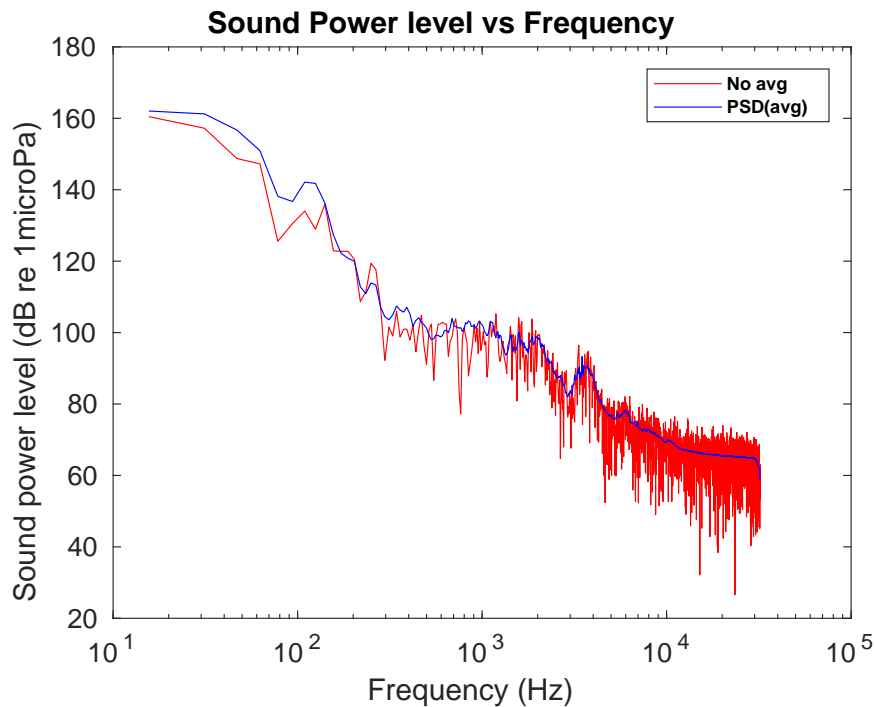


Figure 5.3: Power spectrum created using un-averaged transformed data (red) when compared to an averaged Welch's PSD (blue)

Figure 5.4 shows the spectrogram view for the site DFO-ST at the sampling frequency of 64 kHz. The spectrogram is obtained from the signal Power spectral densities averaged over each individual recording of 7 min duration for the entire period of deployment shown as time in days on the x-axis of Figure 5.4, starting from the deployment date of 24 Aug 2015 till the recovery date of 09 Oct 2015. The spectrogram, helps to visually examine the noise data for long term variations. The spectrogram is displayed with frequencies on the y-axis. The colorbar identifies the intensity of weak and strong signals observed in the data set. The spectrogram demonstrates broad scale temporal patterns only, and because of the averaging involved, it does not display individual signals which are short compared to the averaging time of 7 min. The spectrogram tends to highlight the signal types which are either intense and/or persistent across the averaging time. For example, it is evident that there is lot of high intensity levels present in the lower end of the frequencies ranging between as low as 5 Hz to up to around 500 Hz which is characteristic of typical seismic air gun source levels. The bands seen in this low frequency are the high intensity seismic source noise created as the seismic survey vessel variously approaches the recording location and then subsequently recedes (for example, note this pattern between days 2 and 5).

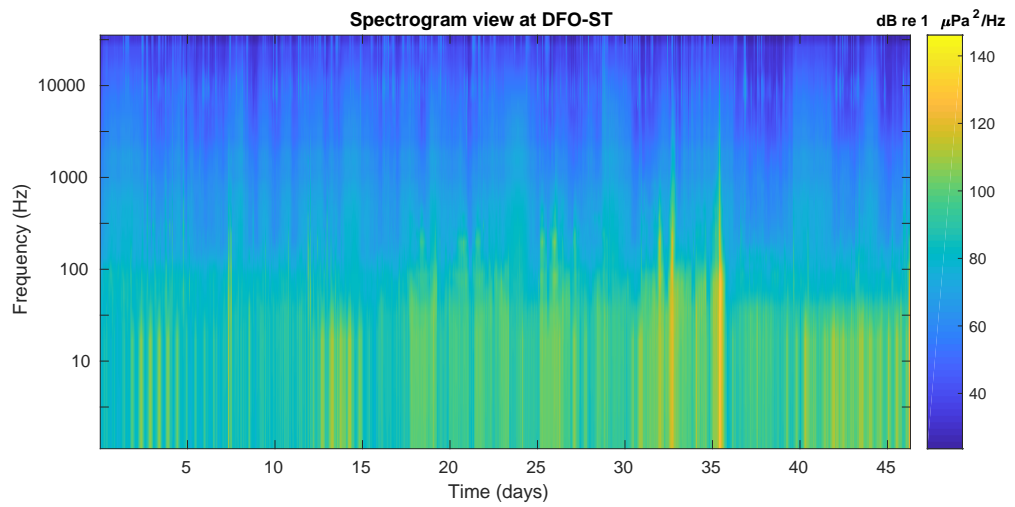


Figure 5.4: Spectrogram view at site DFO-ST

The data from DFO-CT was compared to the data from DFO-ST at sampling frequency 64 kHz to compare the overall Sound Pressure Level (SPL) values with frequencies. As can be seen in Figure 5.5 there is an overall higher level of sound pressure level at DFO-ST for the entire frequency range of interest with higher narrow band noise at 10 kHz up to 32 kHz (which is the maximum resolvable frequency for a sampling frequency of 64 kHz). We notice there is more energy at DFO-CT site between 8 kHz and 10 kHz.

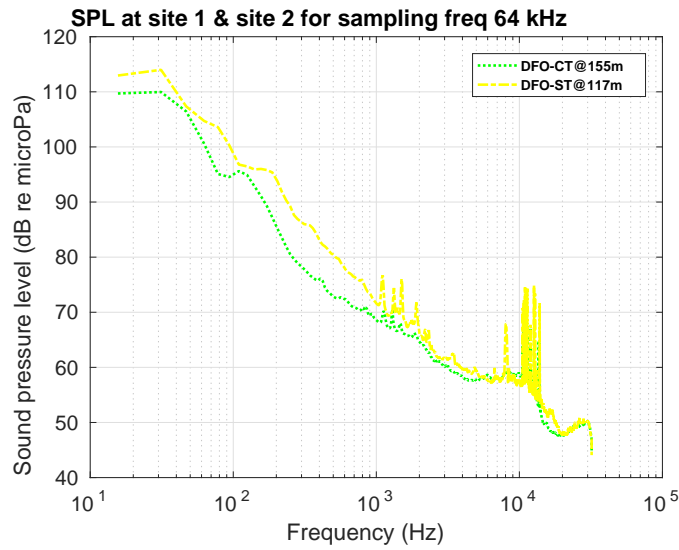


Figure 5.5: Comparison of Sound Pressure Level (SPL) values at sites DFO-CT and DFO-ST for sampling frequency 64 kHz

An overall comparison was also done between the two study sites (DFO-ST and DFO-CT) at the higher sampling rate of 375 kHz. Figure 5.6 compares the Sound Pressure Level (SPL) values at both sites at higher sampling frequency of 375 kHz. Again there is an overall higher level of sound pressure levels at DFO-ST for the entire frequency range with several peaks at the high frequency end due to the biological sound sources like whales and harbour porpoises. We note that in Figure 5.6, above 10 kHz there is a little difference between the two sites except the presence of the spectral peaks (which we attribute to biological noise [37]). It does raise the question as to why the animal activity was greater at the DFO-ST site as compared to the DFO-CT site.

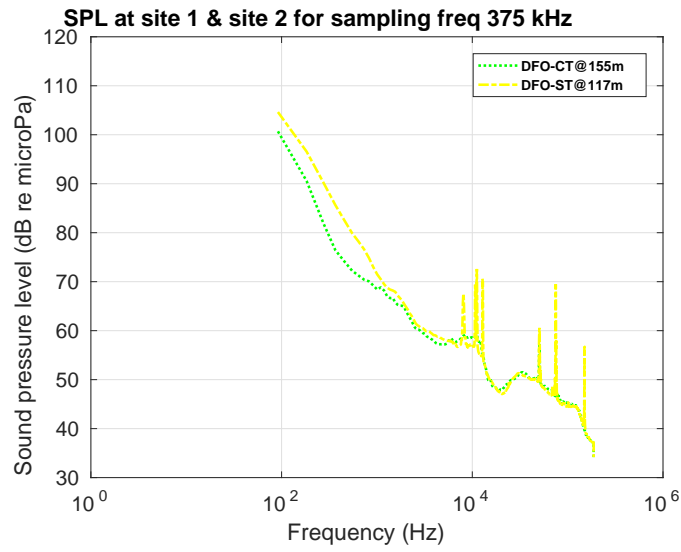


Figure 5.6: Comparison of Sound Pressure Level (SPL) values at sites DFO-CT and DFO-ST for sampling frequency 375 kHz

In order to account for the bottom loss effects, the bottom interaction model response (Refer to chapter 4) was taken into consideration; the response characteristics for the DFO-ST site at sampling frequency 375 kHz is shown in Figure 5.7.

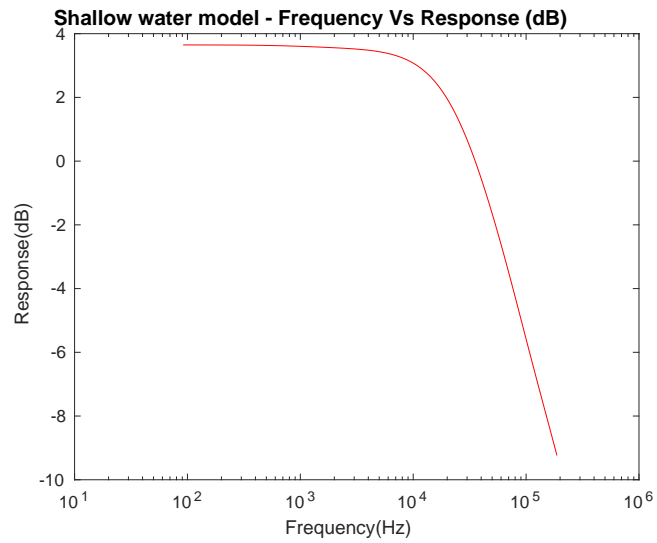


Figure 5.7: Model response in dB for the entire frequency range at site DFO-ST at sampling frequency 375 kHz

In both Figures 5.8 and 5.9, the model response takes into account bottom losses due to the sites being at shallow waters. The resulting sound pressure levels are lowered by 3.7 dB for the range of frequencies spanning from about 100 Hz to about 10 kHz for both sites and there after increase with increase in frequencies as can be seen in both the figures. This increase in sound levels with model correction occurs because sound pressure levels are suppressed at higher frequencies and the model applies a correction for this effect which is most apparent at highest frequencies.

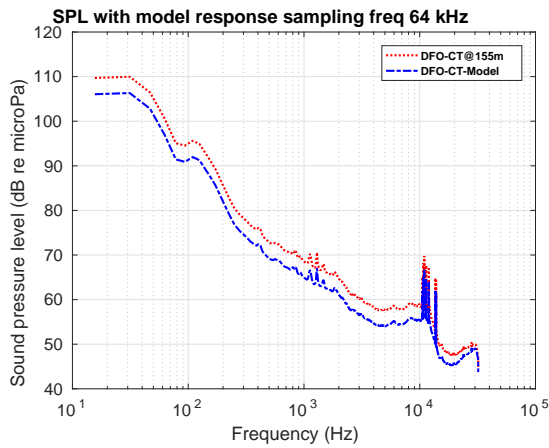


Figure 5.8: Comparison of Sound Pressure Level (SPL) values at site DFO-CT with Model response at sampling frequency 64 kHz

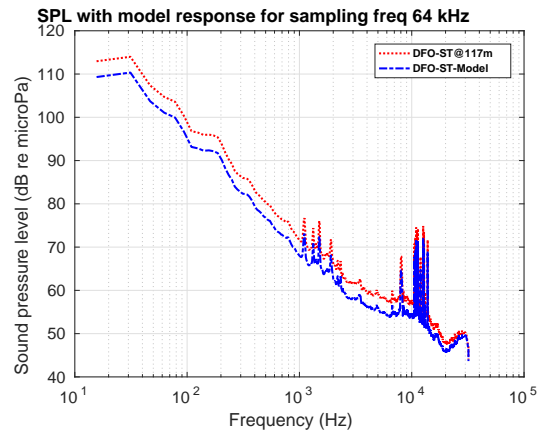


Figure 5.9: Comparison of Sound Pressure Level (SPL) values at site DFO-ST with Model response at sampling frequency 64 kHz

Comparison of model response is repeated with the 375 kHz data in Figures 5.10 and 5.11. It is evident in the both these figures that the model response has enhanced the sound pressure levels at higher frequencies as the levels are up, anywhere from few dB to upto 10 dB for frequencies beyond 50 kHz. But, the model assumes all sounds are generated at the surface and as a result will over-compensate the high frequency biological sounds.

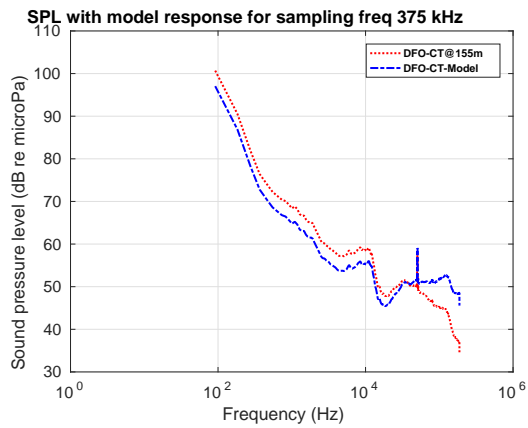


Figure 5.10: Comparison of Sound Pressure Level (SPL) values at site DFO-CT with Model response at sampling frequency 375 kHz

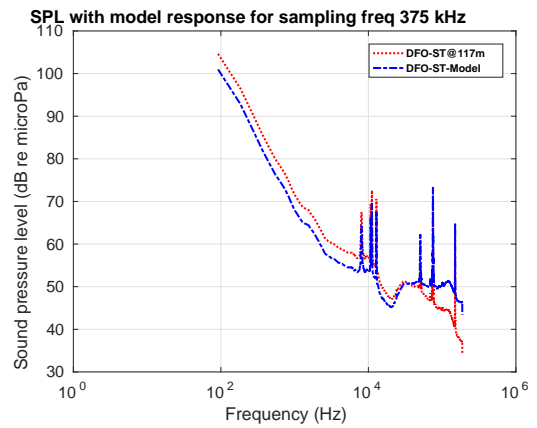


Figure 5.11: Comparison of Sound Pressure Level (SPL) values at site DFO-ST with Model response at sampling frequency 375 kHz

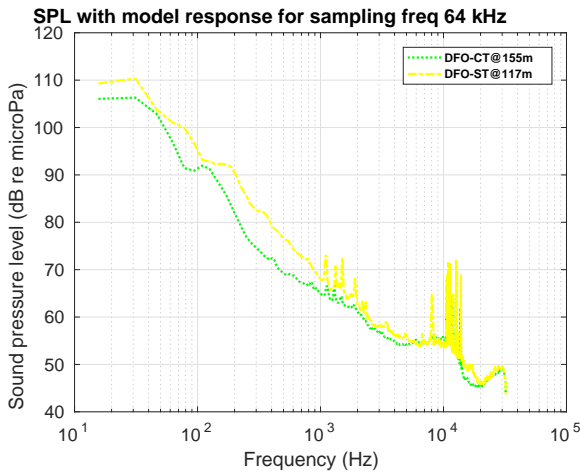


Figure 5.12: Comparison after model response at site DFO-CT (in green) and site DFO-ST for sampling frequency 64 kHz

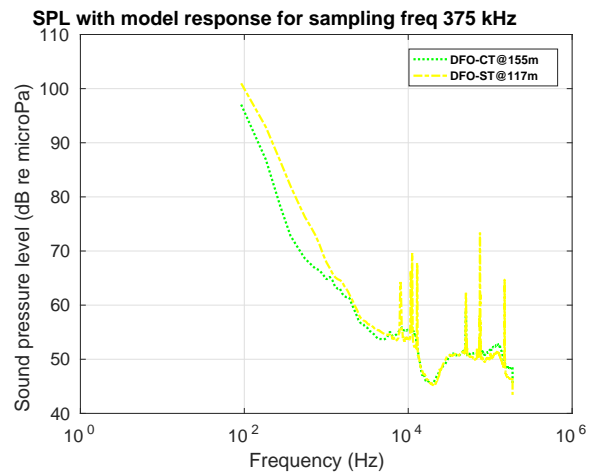


Figure 5.13: Comparison after model response at site DFO-CT and DFO-ST at sampling frequency 375 kHz

Figure 5.12 represents a comparative plot of sound pressure levels at both sites, after accounting for the bottom losses, taking into account the bottom interaction model response at sampling frequency of 64 kHz. The sound pressure levels are higher at DFO-ST site when compared to DFO-CT and that's agreeable to the fact that DFO-ST is closer to seismic survey site under consideration. While, Figure 5.13 represents a comparative plot of sound pressure levels at both sites, after accounting for the bottom losses, taking into account the bottom interaction model response at sampling frequency of 375 kHz. In Figure 5.13, we observe that the sound pressure levels are higher for DFO-ST site at higher frequencies beyond 50 kHz when compared to the DFO-CT.

5.2.1 Averaging method

The basic tools used to analyze the signals are based on statistical analysis: maximum and minimum values, averages, variances and standard deviation. Of all the averaging techniques known, block average is applied when we need to average data in intervals, instead of averaging the entire signal at once. We end up creating an array of means, where each mean is average of a continuous block of samples and each block is of the same size. There are two approaches to the averaging method that were used for the present data analysis. The data set was analyzed for the entire period of deployment and finally 3 hourly averages of the sound pressure levels were compared between the two sites. In order to identify the sources of sound contributing to the ambient noise, Nystuen's weather classification model was used. The 3 hourly averages are shown here for sites DFO-CT and DFO-ST, with and without shallow water corrections to get a comparative analysis. We then compared the 3 hourly averages, after the bottom interaction model corrections

(Figure 5.16 and Figure 5.17), to see if the model makes any difference for the Nystuen plots and we found it made no significant changes to the plots. We therefore show the plots for shipping detection test only, with and without correction. The shallow water model correction at 4 kHz is about 3.5 dB while at 20 kHz is reduced to 2 dB. The difference is about 1.5 dB which doesn't make a significant difference as Nystuen's plots compare levels between two frequencies.

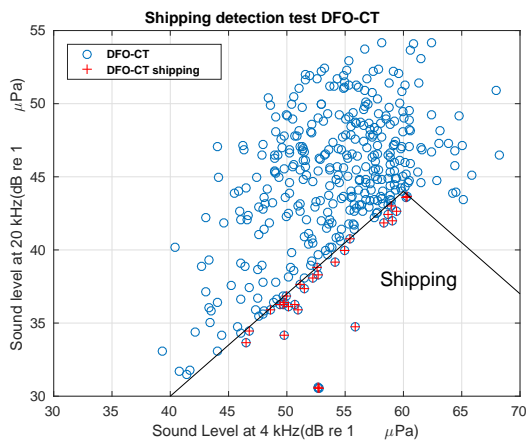


Figure 5.14: 3 hourly averages for shipping contamination detection at DFO-CT (without correction)

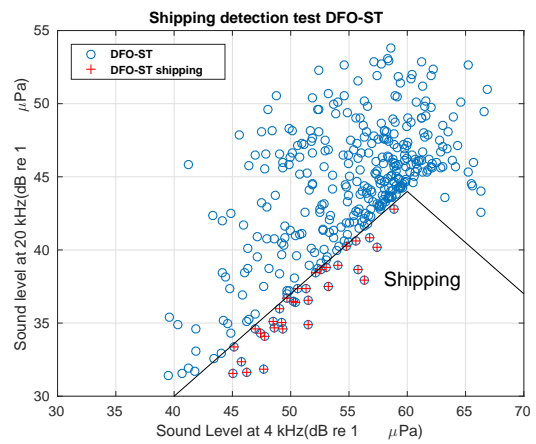


Figure 5.15: 3 hourly averages for shipping contamination detection at DFO-ST (without correction)

Figure 5.14 lacks the clear roll off at 4 kHz sound levels above 60 dB which can be clearly seen in Figure 5.15. This difference suggests that at 20 kHz, site CT has more noisy data than comparable data at site ST.

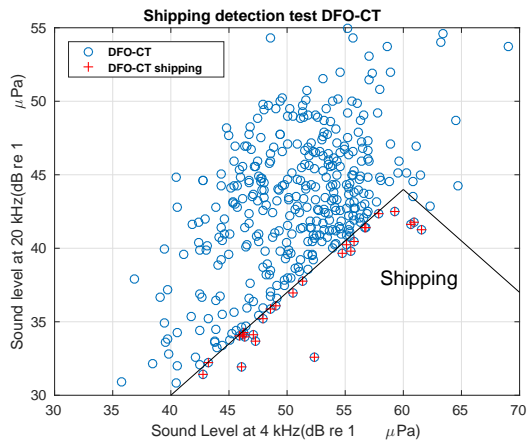


Figure 5.16: 3 hourly averages for shipping contamination detection at DFO-CT (with correction)

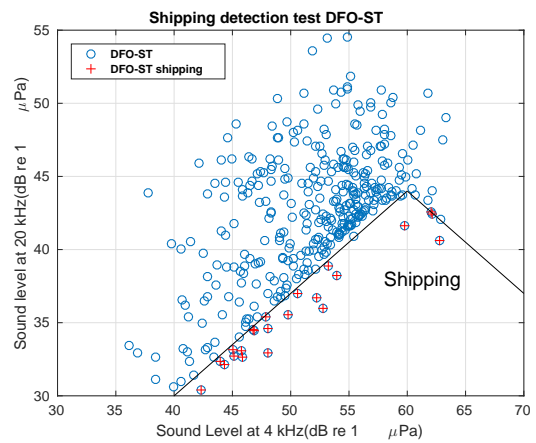


Figure 5.17: 3 hourly averages for shipping contamination detection at DFO-ST (with correction)

In Figure 5.17, we notice the gap between Nystuen’s reference line and the cluster of points which is not evident in the figures without correction. This difference suggests that we are not getting the correction right perhaps.

Each data point in Figure 5.14 and Figure 5.15 represent 3 hourly averages of the sound pressure levels at 4 kHz corresponding to the sound pressure levels at 20 kHz. The data points falling in the region labelled **Shipping** identify as the data points contaminated by shipping and these data have been removed from the entire data. At low wind speeds (lower sound levels), we have sound levels that are too high at 4 kHz compared to what Nystuen (See chapter 3) sees. In other words, our slope of the 20 kHz to 4 kHz is not as steep as Nystuen’s. Definitely, the contamination due to shipping is higher at DFO-ST due to presence of seismic source nearby when compared to the DFO-CT as is evident in Figure 5.14 and Figure 5.15.

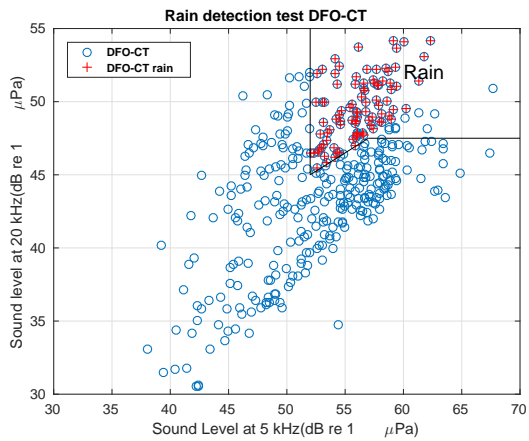


Figure 5.18: 3 hourly averages for rain-fall detection at DFO-CT

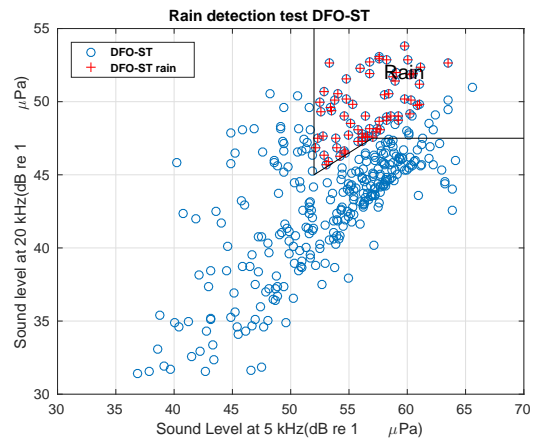


Figure 5.19: 3 hourly averages for rain-fall detection at DFO-ST

Each data point in Figure 5.18 and Figure 5.19 represents 3 hourly averages of the sound pressure levels at 5 kHz corresponding to the sound pressure levels at 20 kHz, respectively. The area labelled **Rain** denotes the data points contributing to heavy rain and have been flagged as Rain for further processing of the data.

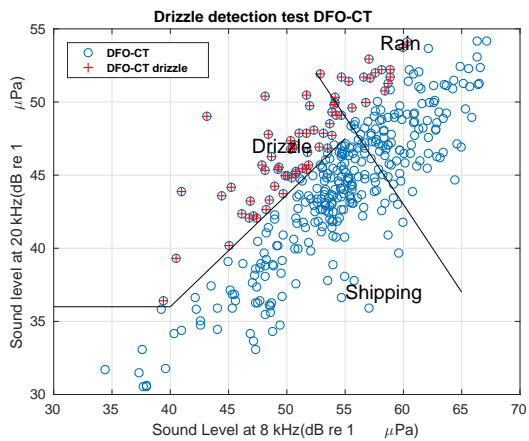


Figure 5.20: 3 hourly averages for drizzle detection at DFO-CT

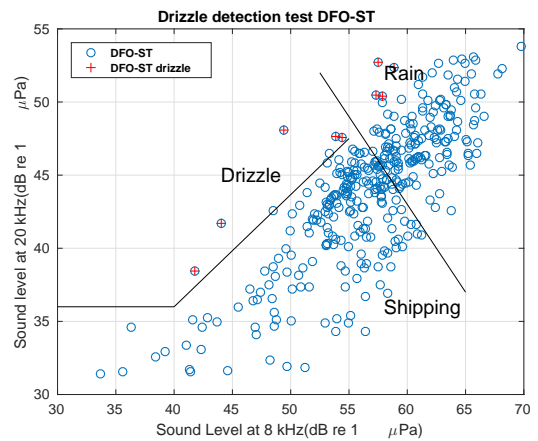


Figure 5.21: 3 hourly averages for drizzle detection at DFO-ST

Each data point in Figure 5.20 and Figure 5.21 represents 3 hourly averages of the sound pressure levels at 8 kHz corresponding to the sound pressure levels at 20 kHz, respectively. It is evident that there are higher occurrences of drizzle and rain in the data at site DFO-CT when compared to site DFO-ST (see Figure 5.5 where site DFO-CT has higher levels at around 8 kHz than site DFO-ST at the said frequency). This difference could probably be associated with larger proportion of the data being flagged as shipping detection. The area labelled **Drizzle** denotes the data points contributing to drizzle and has been flagged as drizzle for further processing of the data.

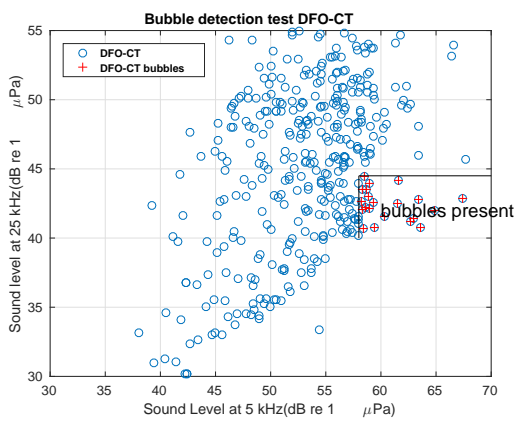


Figure 5.22: 3 hourly averages for bubble detection at DFO-CT

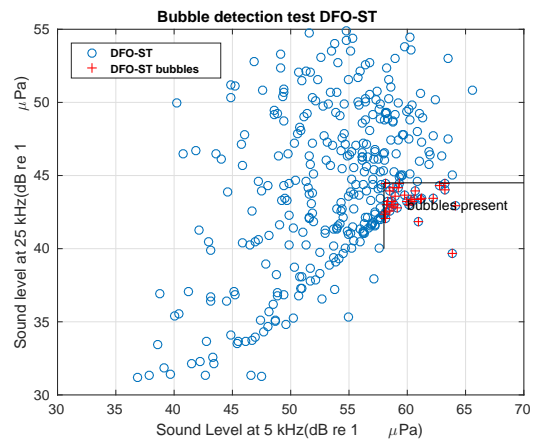


Figure 5.23: 3 hourly averages for bubble detection at DFO-ST

Each data point in Figure 5.22 and Figure 5.23 represents 3 hourly averages of the sound pressure levels at 5 kHz corresponding to the sound pressure levels at 25 kHz, respectively. The area labelled **bubbles present** denotes bubbles are present and has been flagged as bubbles for further processing of the data.

There are higher occurrences of wind with drizzle and rain (blue line of the legend in

Figure 5.24 when compared to the same of Figure 5.26). In order to obtain the wind only (black line of legend in Figures 5.26 and 5.24), the wind speed algorithm [34] is applied at 8 kHz.

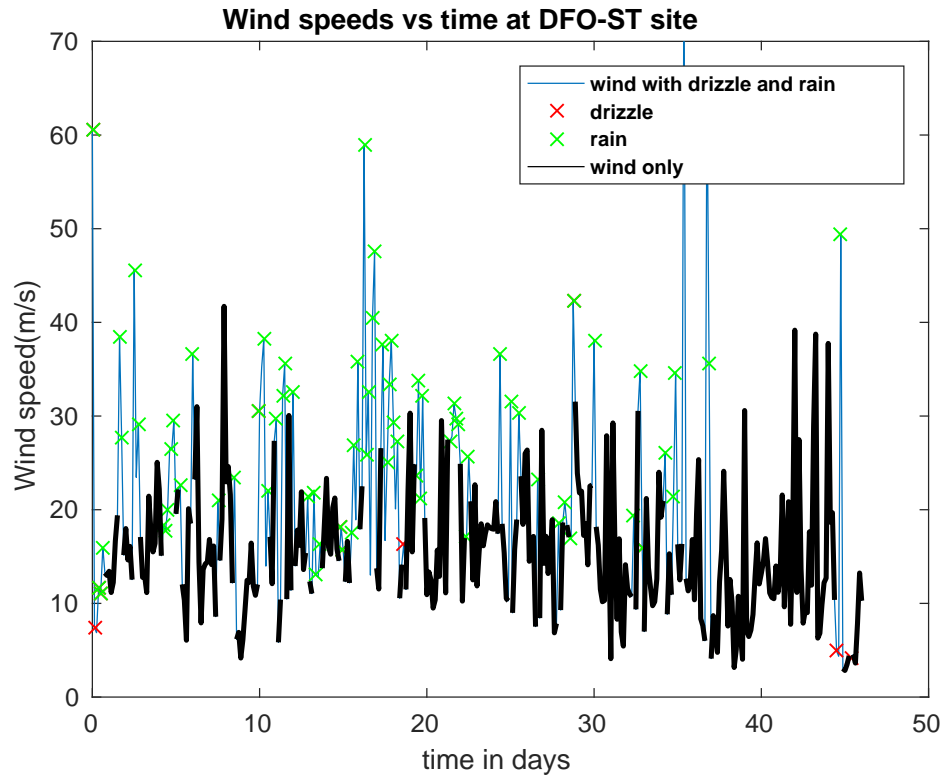


Figure 5.24: Wind speeds vs Time in days at DFO-ST (without bottom interaction model correction)

The bottom interaction model correction yields a correction of around 3 dB that makes a big difference in the wind speed estimates i.e at 10 m/s represented as U10 (m/s) on x-axis of Figure 5.25 which is where the wind speed algorithm is applied, we obtain a consequence of a 3 dB change in wind speed by differentiating equation (see chapter 3 equation 3.7), the result is shown in Figure 5.25. This high sensitivity to adjustment in sound level

makes it unreasonable to use the shallow water correction.

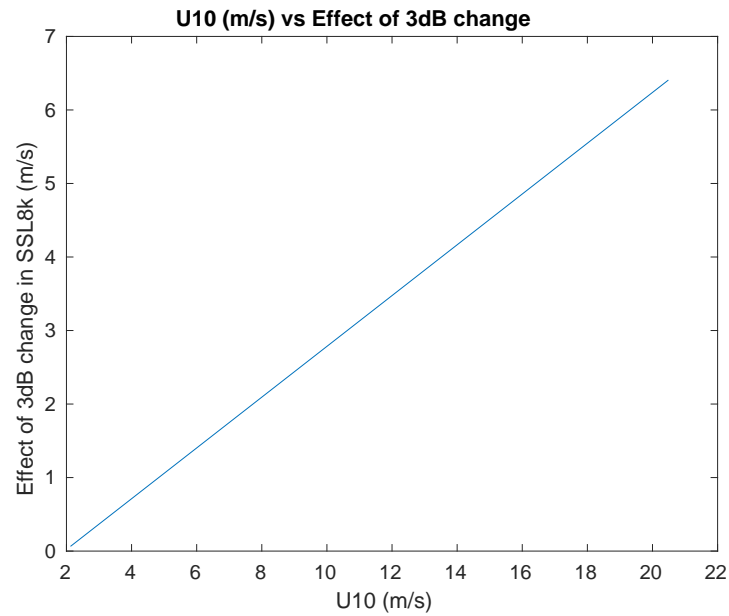


Figure 5.25: U10 (m/s) vs effect of 3 dB change in sound pressure level at 8 kHz

Thus, the 3 hourly averages of the data set were used to plot a graph between wind speeds versus the time in days for site DFO-ST considering the bottom interaction model correction at 8 kHz sound pressure levels only since wind speeds were obtained by applying wind speed algorithm (see chapter 3 equation 3.7) at 8 kHz. Data points for which rain was present are determined after applying rainfall rate algorithm (see chapter 3 equation 3.4) [27], are marked as green x, observations of drizzle are marked as red x and wind only by black line in (Figure 5.26). These wind speeds are further used to compare with the model wind data.

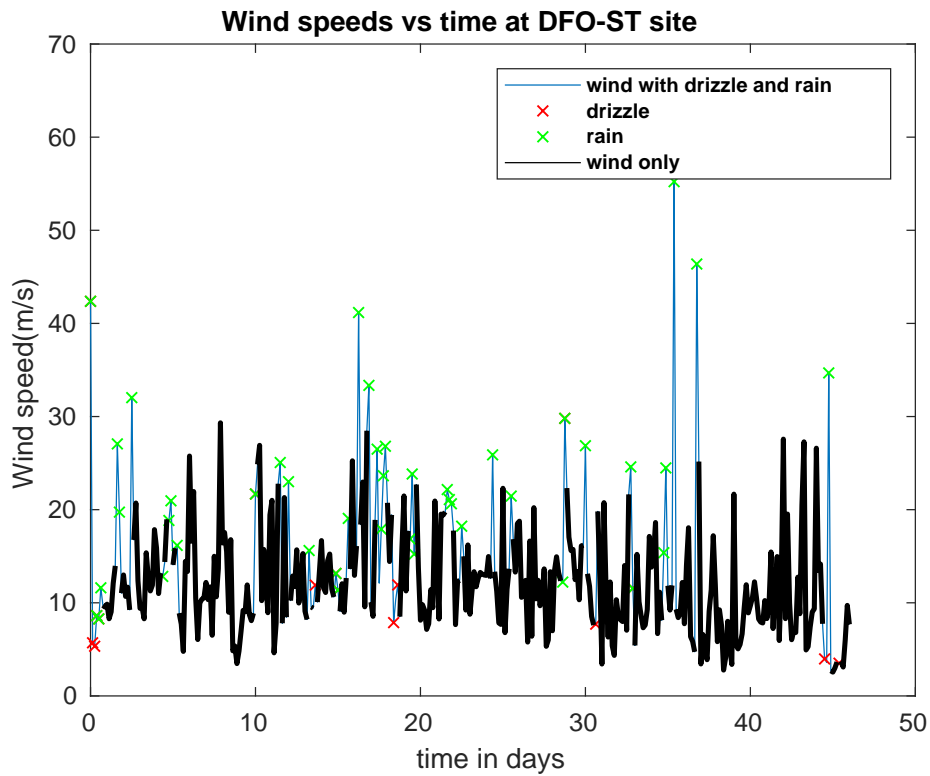


Figure 5.26: Wind speeds vs Time in days at DFO-ST

5.2.2 Standard deviation approach

The fact that there are occurrences of anomalously high wind speeds in the processed estimates (Refer Figure 5.26), directed us to get a deeper understanding of their origin. Our goal is not to identify the highest sound levels which might be caused by transient events but rather the background natural sound. With that goal, we chose to measure the standard deviation of sound levels in each data set which was then sorted to identify the outliers. We set different *threshold* values and experimented as to which value would work best to meet our goal of eliminating the outliers. Hence, we set different threshold values like *one quarter*, *one half* and *three quarters* of the total number of values of the standard devia-

tion. Setting a threshold value of *one half* of the total number of values worked best and hence discarded the outliers. Shipping noise, seismic survey noise and noises from biological sources are transient, compared to the ambient noise which varies on much longer time scales suggesting that the elimination of infrequent high level events can remove this contamination while leaving the slowly varying wind and rain sounds.

A low standard deviation indicates that the sound levels tend to be uniform during the sample period, while a high standard deviation indicates that the sound levels spread out over a wider range of values. Using this feature of standard deviation, we then associate higher standard deviation levels with bad data and before calculating the PSDs, sorted data by standard deviation as shown in Figure 5.27.

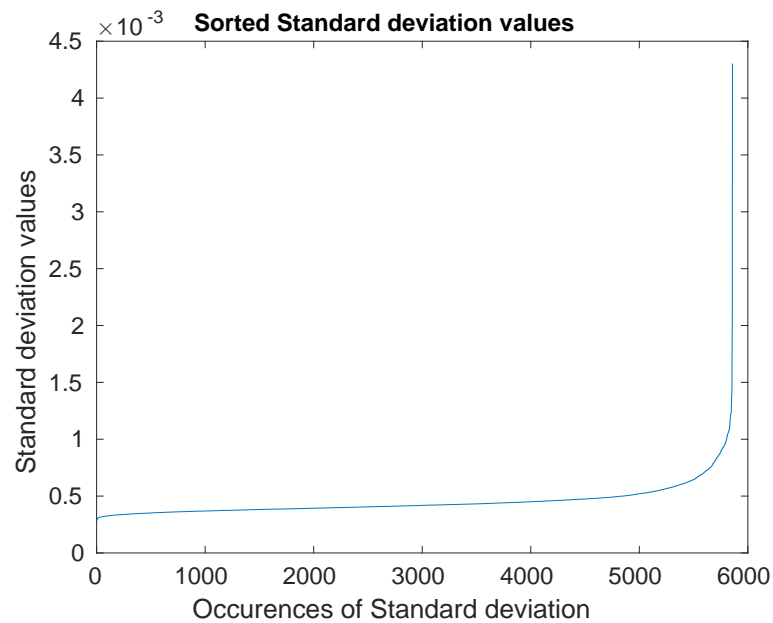


Figure 5.27: Standard deviation plot sorted from low to high values

Clearly the values of standard deviation that are very high towards the right end of the

x-axis are the outliers and major contributors to the narrow band noise found in the PSD (see Figure 5.4 at frequencies around 8 kHz where we clearly see variability caused by seismic activity). We arbitrarily set a threshold value at the level of half the total number of values discarding the outliers that have threshold values above 0.4×10^{-3} volts. We calculate the signal level standard deviation for each of the sub-intervals and it is these values that we sort to identify the least likely contaminated data. The PSD for any hour time interval was calculated using the remaining sub-intervals. Data processed in this way for the entire period of deployment obtains much reduced narrow band noise at higher frequencies (See Figure 5.28 at around 8 kHz and compare to Figure 5.5).

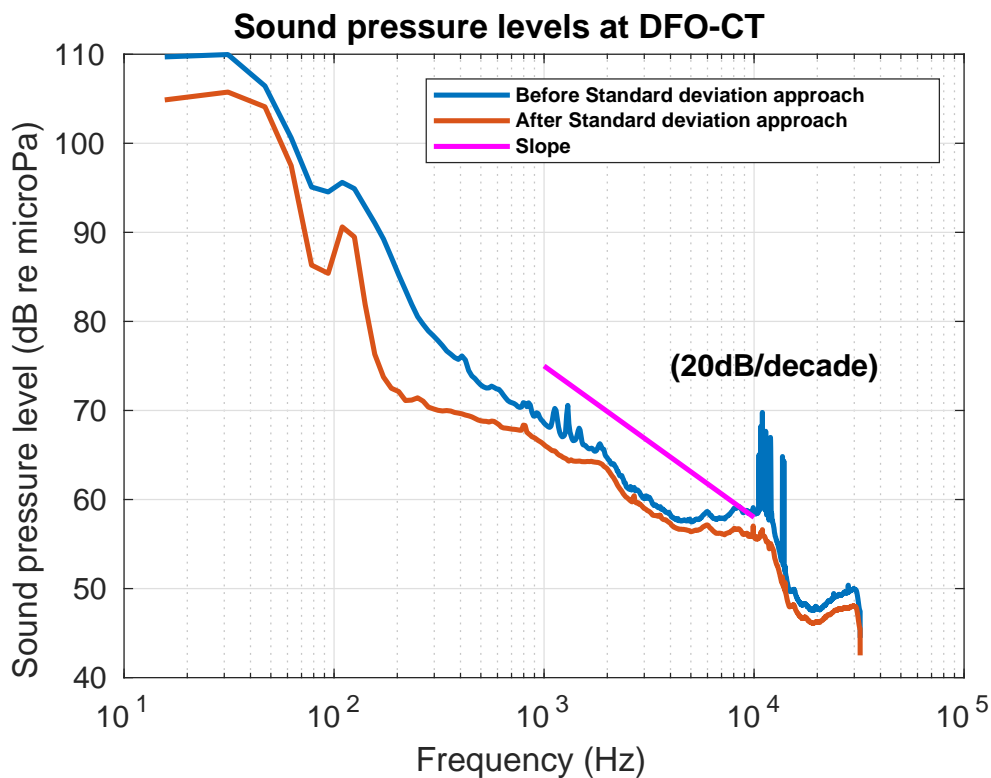


Figure 5.28: DFO-CT sound pressure levels before and after the Standard deviation approach (sampling frequency 64 kHz)

Figure 5.28 shows the results of standard deviation analysis on the 64 kHz sample frequency data for site DFO-CT obtaining sound pressure levels before and after the standard deviation approach for the entire period of deployment. We have eliminated most of the narrow band noise at higher frequencies around 8 to 10 kHz and beyond, yet the overall shape of the ambient noise curve is retained with only a modest decrease in level.

5.2.3 Comparison with GDPS (Global Deterministic Prediction System) wind model data

We were looking for the oceanic wind data for the period of interest, August 2015 to November 2015. This is a period for which weather buoys were not reporting. We were provided with a 25 km resolution wind model data (which was developed and produced by Environment Canada operationally) by Department of Fisheries and Oceans, Canada, Newfoundland. The Environment Canada's GDPS (Global Deterministic Prediction System) Model data was used for this purpose. After detection of rain and ship events, the noise level based wind speeds provide a smoothly varying record. However, we need an independent measure of wind speed against which we can compare the present results. Hence, the model wind data was used for this purpose.

The data was provided as a netcdf file which has a $1/12^{\circ}$ resolution and is 3 hourly wind data. The data was provided for the period starting Aug 1st till Nov 30th 2015. We chose the period to overlap with winds when the deployment was done at Grand Banks which was August 24th till October 9th 2015 and were interpolated to the definite latitude and longitude of interest. The three hourly averages were calculated for the recorded data at sites DFO-CT and DFO-ST. The model wind speeds and the speeds obtained after applying

wind speed algorithm [34] to control site data (DFO-CT) are shown in Figure 5.29. There is a fair agreement between the model wind speed and that obtained after applying the wind speed algorithm, beginning from day 10 till day 35 and continues again to be in fair agreement from day 35 till the end of deployment. For the study site (DFO-ST shown in Figure 5.30), we suspect that as the study site is closer to the seismic survey work, it leads to higher sound pressure levels due to seismic noise not removed from our data processing, when compared to the DFO-CT site.

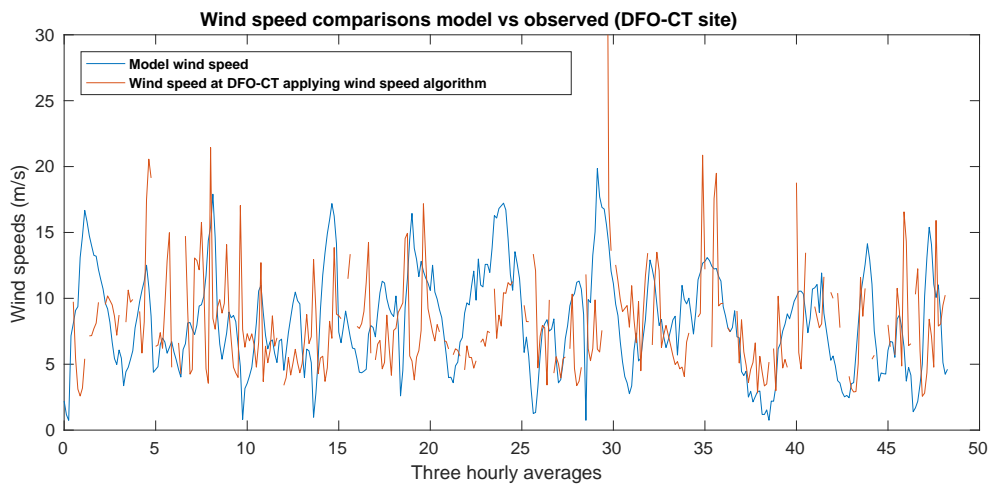


Figure 5.29: Model wind speeds vs observed at DFO-CT

In order to understand the apparent bias in wind speed estimates, the comparison was repeated without considering the bottom interaction model corrections. Figure 5.31 shows how the three hourly averages compare for model wind speed vs the wind speed at DFO-CT after applying the wind speed algorithm to our un-correlated data.

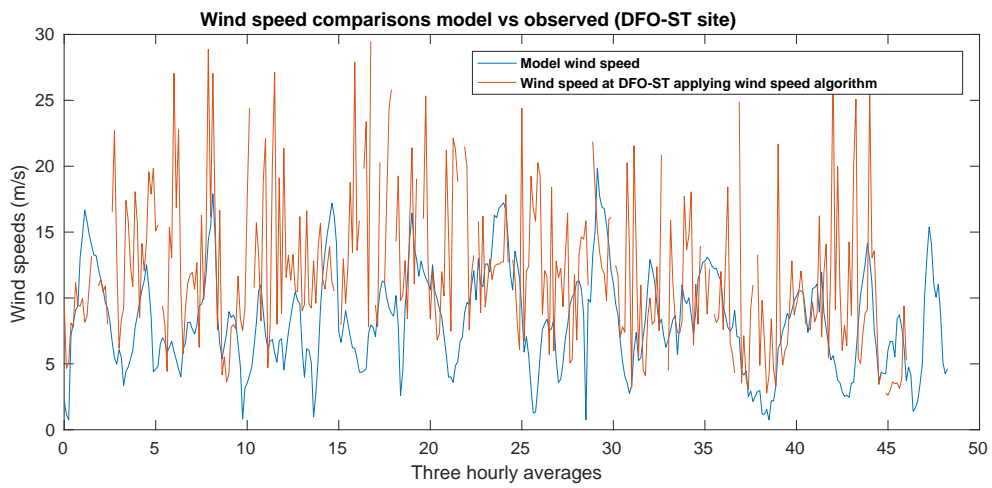


Figure 5.30: Model wind speeds vs observed at DFO-ST

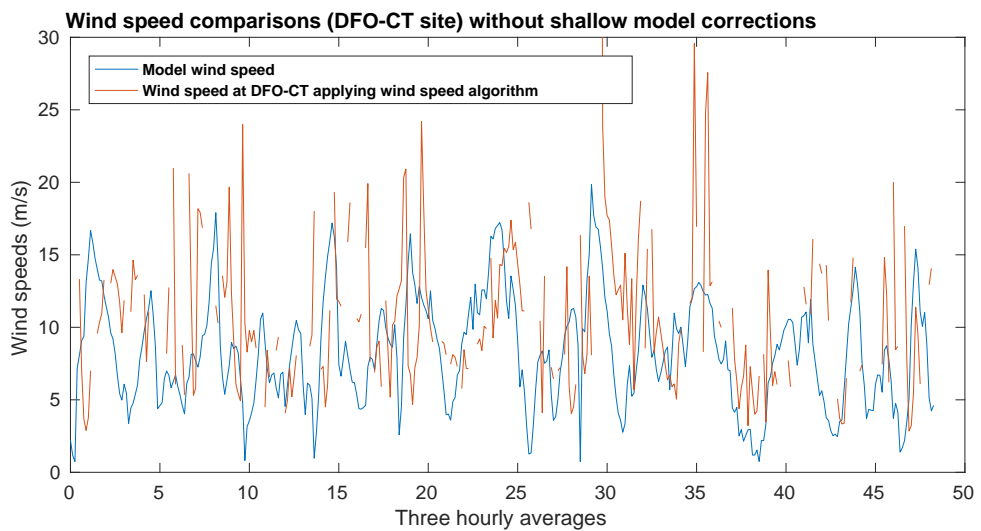


Figure 5.31: Model wind speeds vs observed at DFO-CT without bottom interaction model corrections

In order to quantify for the level comparisons, we chose to do scatter plots of the wind speeds for site DFO-CT with and without bottom interaction model corrections. Figure

5.32 and Figure 5.33 represent a scatter plot comparing the wind speeds at DFO-CT with and without bottom interaction model corrections respectively.

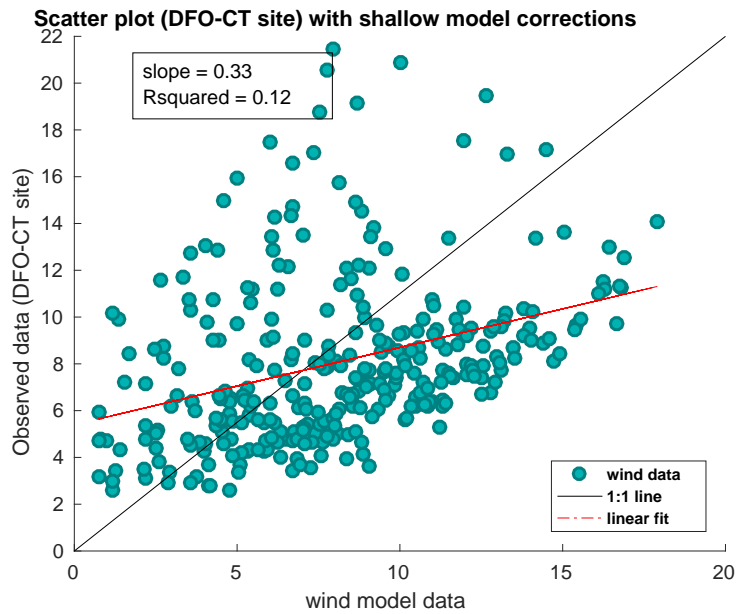


Figure 5.32: Scatter plot comparing wind speeds at DFO-CT

For Figure 5.32, a 1:1 line as well as a linear fit are shown in the figure to observe any correlation. It is clear that there is a correlation but that is not strong. The equation of the linear fit is $y = 0.33 * x + 5.4$, where 0.33 is the slope of the fit as indicated in Figure 5.32. The slope differs from 1 (1 being the slope of ideal linear fit) by 0.67. The goodness of fit (a.k.a Rsquared) being 0.12. The goodness of fit is a statistic measure of how successful the fit is in explaining the variation of the data, with a value closer to 1 indicating a greater proportion of variance is accounted for by the model. Figure 5.32 shows a well defined clustering of points, but they lie below the linear fit line. We accept the bias of the high level anomalies likely because of the many data outliers which are high in the DFO-CT data. We

notice that there are essentially NO low speed estimates indicating that the problems here are caused by "noise" rather than just a bad algorithm. If we could do a better job of identifying the bad data, we would get better results. There are two possible ways the sound levels could be reduced: our correction for shallow water could be too great or, our use of standard deviation to eliminate data may be arbitrarily reducing spectral levels.

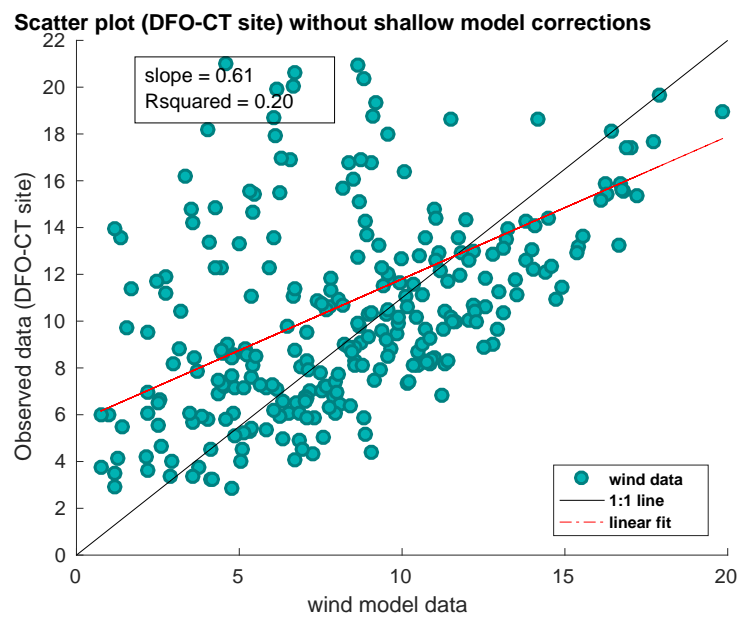


Figure 5.33: Scatter plot comparing wind speeds at DFO-CT without bottom interaction model corrections

The corresponding scatter plot for uncorrected data is shown in Figure 5.33. The scatter points are clearly closer to the linear fit line as well as the 1:1 line, than when data was corrected with the shallow water model (See Figure 5.32). The equation of the linear fit is $y = 0.61 * x + 5.7$, where 0.61 is the slope of the fit as indicated in Figure 5.33. The slope differs from 1 (1 being the slope of ideal linear fit) by 0.39. The goodness of fit (a.k.a Rsquared) being 0.2. The higher value of goodness of fit in this case could probably

be due to the fact that we have been using the bottom interaction model corrections to obtain the actual sound pressure levels. In fact, it seems we could be over estimating the data for representative sound pressure levels at the site of interest. Hence, probably taking into account the bottom interaction model corrections is reducing the sound pressure levels too much. It therefore suggests that sound in reality may not have undergone much of the bottom and surface reflections at this shallow water site when compared to what we assumed to begin with by considering the bottom interaction model. That would occur if bottom and surface reflections were weak.

Chapter 6

Conclusions

This thesis aims to establish baseline underwater sound levels in a region of the Grand Banks and to identify the natural variations contributed by rain, wind and drizzle. Wind speed estimates (obtained by applying the Nystuen wind speed algorithm [34]) are compared with the wind model data provided by Department of Fisheries and Oceans (DFO) Newfoundland for the region of study.

In chapter 3, Nystuen's weather classification algorithm is explained to categorize the ambient sound contributed by shipping, rain, drizzle and ambient bubbles by incorporating the various test conditions under each category. The fact that different underwater sound sources have different spectra, was explained more explicitly in chapter 3. The basic approach to Nystuen's algorithm was to identify sound sources like wind, rain, drizzle and shipping. Ships are known to increase the low frequency sound level more relative to the high frequency levels. Hence, shipping can be detected. Rain on the other hand is known to produce high levels of sound at all frequencies especially over 10 kHz. The presence of heavy rain though obscures the wind-generated sound (breaking waves) and hence a good

estimate of wind speed cannot be obtained. However, drizzle is known to increase the high frequencies (13 kHz and above). Hence, drizzle detection does not hinder the acoustical wind speed measurements.

The main objective of Chapter 4, was to address the naturally occurring effects that result from bottom reflections and acoustic absorptions. The effects of surface and bottom have been investigated with a simple analytical model of ocean ambient sound generation at the surface by incorporating image sources (Refer Figure 4.2 from Chapter 4) to represent reflections. The effects of refraction have not been considered. One of the striking results of the modeling has been that at low frequencies, significant increases in sound levels can occur even for a deep ocean (Refer Figure 4.3 from Chapter 4). Signal level enhancements of several dB can occur typically at frequencies below 10 kHz.

In Chapter 5, data from Grand Banks was analyzed. Two data sets were available for the two sites of interest. The data from both the sites, DFO-CT and DFO-ST, were studied and wind speeds were obtained for the entire data set for the period of deployment. Three hourly averages of the sound pressure levels were obtained from the entire data set and the sound pressure levels corresponding to shipping, rain, drizzle and ambient bubbles were identified for both the sites and flagged accordingly. The bottom interaction model correction at 4 kHz is about 3.5 dB while at 20 kHz is reduced to 2 dB. The difference is about 1.5 dB which doesn't make a huge difference as the Nystuen's plots are plotted taking sound pressure levels at one frequency versus another frequency. Hence we discussed the results for shipping detection test for both sites, with and without bottom interaction model corrections and found that the model does not make any significant changes to the plots. The data points associated with shipping, drizzle and rain have been removed from the entire data set in order to identify the contribution from wind alone. Thus, the obtained

sorted data was compared with the model wind data. Initial survey of data quality showed the occurrence of transient high energy pulses present over a narrow band of frequencies at both the sites. The overall spectral shape of the ambient noise at both the sites followed the shape of Wenz's standard ambient spectral shape (Refer Chapter 2 Figure 2.5). The sound pressure levels at the DFO-ST were higher by few decibels, overall, when compared to that at DFO-CT (Refer Chapter 5 Figure 5.5). After correcting the data using the bottom interaction model corrections, the sound pressure levels seem to compare well at both the sites.

The occurrences of anomalously high wind speeds in the processed estimates directed us to get a deeper understanding. With that perspective, we chose to measure the standard deviation of sound levels in each data set and sort them to identify the outliers. Standard deviation approach proved to be a good approach to understand the occurrences of very high wind speeds, owing to the fact that there were transient high energy pulses in narrow band frequencies at both the sites. We set different *threshold* values and experimented as to which value would work best to meet our goal of eliminating the outliers. Hence, we set different threshold values like *one quarter*, *one half* and *three quarters* of the total number of values of the standard deviation. Setting a threshold value of *one half* of the total number of values worked best and hence discarded the outliers. We obtained the sound pressure levels without the narrow band noise at higher frequencies while retaining the overall shape of the ambient noise (Refer Chapter 5 Figure 5.28).

Scatter plots were drawn for the three hourly averages of the wind speeds that were obtained by applying the wind speed algorithm [34] and that obtained from the model wind data provided by DFO. The values at site DFO-CT compare well with the linear fit line but points seem to cluster somewhat below the fit line indicating that the acoustic derived wind

speeds are low, with 0.33 being the slope of the fit. The slope differs from 1 (1 being the slope of ideal linear fit) by 0.67. The goodness of fit (a.k.a Rsquared) being 0.12. We accept the bias of the high level anomalies likely because of the many data outliers which are high in the DFO-CT data (Refer Chapter 5 Figure 5.32). We notice that there are essentially NO low speed estimates indicating that the problems here are caused by "noise" rather than just a bad algorithm. If we could do a better job of identifying the bad data, we would get better results.

The DFO-CT scatter plot was redrawn without considering the bottom interaction model corrections (Refer Chapter 5 Figure 5.33); data points appear better aligned with the linear fit line as well as the 1:1 line with 0.61 being the slope of the fit. The slope differs from 1 (1 being the slope of ideal linear fit) by 0.39. The goodness of fit (a.k.a Rsquared) being 0.2. The higher value of goodness of fit in this case could probably be due to the fact that we have been using the bottom interaction model corrections to obtain the actual sound pressure levels. In fact, it seems we could be over estimating the data for representative sound pressure levels at the site of interest.

Thus, we conclude by saying that this research aimed to bring the comparison of wind speeds, which are the natural contributors to the ambient noise, at the sites of interest and there was a good correlation of the wind speeds when compared to the model wind data. The overestimation of the sound pressure levels by considering the bottom interaction model leads to further discussion of how important and valid is the model for the sites and leaves scope for future work in this area.

Bibliography

- [1] V. C. Anderson. Arrays for the investigation of ambient noise in the ocean. *The Journal of the Acoustical Society of America*, 30(5):470–477, 1958.
- [2] R. K. Andrew, B. M. Howe, J. A. Mercer, and M. A. Dzieciuch. Ocean ambient sound: comparing the 1960s with the 1990s for a receiver off the california coast. *Acoustics Research Letters Online*, 3(2):65–70, 2002.
- [3] E. M. Arase and T. Arase. Ambient sea noise in the deep and shallow ocean. *The Journal of the Acoustical Society of America*, 42(1):73–77, 1967.
- [4] P. T. Arveson and D. J. Vendittis. Radiated noise characteristics of a modern cargo ship. *The Journal of the Acoustical Society of America*, 107(1):118–129, 2000.
- [5] W. W. Au and R. R. Fay. *Hearing by whales and dolphins*, volume 12. Springer Science & Business Media, 2000.
- [6] D. R. Barclay and M. J. Buckingham. Depth dependence of wind-driven, broadband ambient noise in the philippine sea. *The Journal of the Acoustical Society of America*, 133(1):62–71, 2013.

- [7] Board. Ocean noise and marine mammals, ocean studies and national research council and others, 2003.
- [8] J. W. Cooley and J. W. Tukey. An algorithm for the machine calculation of complex fourier series. *Mathematics of computation*, 19(90):297–301, 1965.
- [9] O. I. Diachok and R. S. Winokur. Spatial variability of underwater ambient noise at the arctic ice-water boundary. *The Journal of the Acoustical Society of America*, 55(4):750–753, 1974.
- [10] R. E. Francois and G. R. Garrison. Sound absorption based on ocean measurements: Part i: Pure water and magnesium sulfate contributions. *The Journal of the Acoustical Society of America*, 72(3):896–907, 1982.
- [11] L. M. Gray and D. S. Greeley. Source level model for propeller blade rate radiation for the worlds merchant fleet. *The Journal of the Acoustical Society of America*, 67(2):516–522, 1980.
- [12] M. H. *Sounds in the Sea: From Ocean Acoustics to Acoustical Oceanography*. Cambridge University Press, 2005.
- [13] D. Hlne and W. Alain. A model to estimate the density, characteristic surface, and coverage of whitecaps using underwater sound. *Journal of Geophysical Research: Oceans*, 98(C10):18213–18219, 1993.
- [14] V. O. Knudsen, R. S. Alford, and J. W. Emling. Underwater ambient noise. *Journal of Marine Research*, 7:410–429, 1948.
- [15] W. Kuperman and P. Roux. *Underwater Acoustics*. Springer New York, 2007.

- [16] E. D. L., W. D. Randolph, H. David, and B. Susan. Oceanic winds measured from the seafloor. *Journal of Geophysical Research: Oceans*, 89(C3):3457–3461, 1984.
- [17] A. Langley. Acoustic emission from the arctic ice sheet. *The Journal of the Acoustical Society of America*, 85(2):692–701, 1989.
- [18] D. D. Lemon, D. M. Farmer, and D. R. Watts. Acoustic measurements of wind speed and precipitation over a continental shelf. *Journal of Geophysical Research: Oceans*, 89(C3):3462–3472, 1984.
- [19] X. Lurton. The range-averaged intensity model: A tool for underwater acoustic field analysis. *IEEE journal of oceanic engineering*, 17(1):138–149, 1992.
- [20] B. B. Ma, J. A. Nystuen, and R.-C. Lien. Prediction of underwater sound levels from rain and wind. *The Journal of the Acoustical Society of America*, 117(6):3555–3565, 2005.
- [21] H. Medwin and M. M. Beaky. Bubble sources of the knudsen sea noise spectra. *The Journal of the Acoustical Society of America*, 86(3):1124–1130, 1989.
- [22] H. Medwin and C. Clay. *Acoustical Oceanography Principles and Applications*. Wiley-Interscience publication, 1997.
- [23] H. Medwin, J. A. Nystuen, P. W. Jacobus, L. H. Ostwald, and D. E. Snyder. The anatomy of underwater rain noise. *The Journal of the Acoustical Society of America*, 92(3):1613–1623, 1992.
- [24] W. K. Melville, M. R. Loewen, C. Francis, T. Andrew, and M. Buckingham. Acoustic and microwave signatures of breaking waves. *Nature*, 336:54–56, 1988.

- [25] J. A. Nystuen. Validation of acoustic measurements of wind and precipitation using expendable ambient noise sensor (ans) drifters, an/wsq-6 (xan-2). Technical report, WASHINGTON UNIV SEATTLE APPLIED PHYSICS LAB, 1997.
- [26] J. A. Nystuen and D. M. Farmer. The influence of wind on the underwater sound generated by light rain. *The Journal of the Acoustical Society of America*, 82(1):270–274, 1987.
- [27] J. A. Nystuen, C. C. McGlothlin, and M. S. Cook. The underwater sound generated by heavy rainfall. *The Journal of the Acoustical Society of America*, 93(6):3169–3177, 1993.
- [28] A. J. Perrone. Ambient-noise-spectrum levels as a function of water depth. *The Journal of the Acoustical Society of America*, 48(1B):362–370, 1970.
- [29] M. B. Porter. The bellhop manual and users guide: Preliminary draft. *Heat, Light, and Sound Research, Inc., La Jolla, CA, USA, Tech. Rep*, 2011.
- [30] D. Ross. *Mechanics of underwater noise*. Permagon Press, 1976.
- [31] C. Shank. The committee on the status of endangered wildlife in canada(cosewic): A 21-year retrospective. *Canadian Field-Naturalist*, 113(2):318–341, 1999.
- [32] M. V. Trevorrow, T. Yamamoto, A. Turgut, D. Goodman, and M. Badiy. Very low frequency ocean bottom ambient seismic noise and coupling on the shallow continental shelf. *Marine geophysical researches*, 11(2):129–152, 1989.
- [33] R. Urick. *Principles of Underwater Sound*. McGraw Hill Book company, 1975.

- [34] S. Vagle, W. G. Large, and D. M. Farmer. An evaluation of the wotan technique of inferring oceanic winds from underwater ambient sound. *Journal of Atmospheric and Oceanic Technology*, 7(4):576–595, 1990.
- [35] G. M. Wenz. Acoustic ambient noise in the ocean: Spectra and sources. *The Journal of the Acoustical Society of America*, 34(12):1936–1956, 1962.
- [36] Y. Xie and D. M. Farmer. The sound of ice break-up and floe interaction. *The Journal of the Acoustical Society of America*, 91(3):1423–1428, 1992.
- [37] L. Zedel and K. Angadi. Private communication with JASCO Applied Sciences (Canada) Ltd, 2018.